arXiv:2607.01407v1 [cond-mat.mtrl-sci] 1 Jul 2026

`Vitriflow`: calibrated amorphous structure ensembles from melt–quench simulations

Jonathon Cottom[a,b], Robin Delhomme[a,b], Emilia Olsson[a,b,*]

[a] *Institute for Theoretical Physics, University of Amsterdam, Science Park 904, Amsterdam, 1098 XH, the Netherlands*
[b] *Advanced Research Center for Nanolithography, Science Park 106, Amsterdam, 1098 XG, the Netherlands*

Abstract

Melt–quench molecular dynamics is widely used to construct amorphous materials models, but the resulting ensemble is defined by choices that are often made implicitly: numerical settings, melt temperature, liquid-hold time, quench rate, system size, and post-generation screening. We introduce `Vitriflow`, a computational materials methodology that turns these choices into an explicit decision chain. The framework couples numerical stability, descriptor-based protocol calibration, user-defined artefact screening, and statistical convergence of the generated analysis ensemble in a material-specific descriptor space. We demonstrate the approach for a-SiO_2, a-Si_3N_4, and a-Sm_2O_3, which respectively test tetrahedral network fidelity, MG2 $\rightarrow$ PBE $\rightarrow$ HSE06 DFT refinement of a heteropolar nitride, and amorphous/crystal discrimination in a mixed-coordination rare-earth oxide. `Vitriflow` separates defect-free from oxygen-bridge-defective silica, quantifies DFT-refinement response in a common a-Si_3N_4 structural population, and removes recrystallised Sm_2O_3 structures without imposing fixed coordination. The result is a reproducible route for generating amorphous ensembles whose numerical settings, thermal protocol, screening actions, and statistical precision are selected from the materials question rather than assumed *a priori*.

Keywords: amorphous materials, melt–quench, molecular dynamics, reproducibility, protocol calibration, ensemble convergence

*Corresponding author.
Email address: `k.i.e.olsson@uva.nl` (Emilia Olsson)

1. Introduction

Amorphous oxides, nitrides, and semiconductors underpin a wide range of dielectric, optical, electronic, and protective thin-film technologies.[1, 2, 3, 4, 5, 6, 7, 8, 9] Their key observables—density, coordination statistics, medium-range topology, defect populations, and the properties derived from them—are structural and cannot be specified by a small unit cell and a set of symmetry labels.[10, 11, 12, 13] Atomistic simulation is therefore often required to construct structural models that can be connected directly to diffraction, spectroscopy, transport, interfacial ion migration, and mechanical response.[14, 15, 16, 17, 18] At the same time, the absence of long-range periodicity makes amorphous materials intrinsically difficult to model, and a persistent gap remains between laboratory structures and the configurations accessible on atomistic time and length scales.[19, 20, 21, 22, 23]

Among available atomistic routes, melt–quench molecular dynamics is one of the most broadly applicable methods for constructing amorphous models with empirical interatomic potentials, *ab initio* electronic structure forces, or machine-learned interatomic potentials.[22, 24, 25, 26, 27, 28, 29, 30] For network glasses such as a-SiO_2, it is a plausible proxy for vitrification;[31, 32, 33] for non-glass-forming systems, it is better understood as a controlled route to disordered structural models than as a literal representation of synthesis.[19, 20, 21] The nominal protocol is simple: heat above the temperature at which crystalline memory is lost, equilibrate the liquid, cool to the target temperature, and relax. In practice, however, the final amorphous state is path dependent. In silica, cooling rate and system size alter density, coordination, bond-angle distributions, ring statistics, and intermediate-range structural signatures such as the first sharp diffraction peak.[31, 33, 34, 35, 32, 25, 36, 15, 37] In amorphous Si_3N_4 and amorphous Si, both defect content and network topology depend on preparation route and on the chosen interaction model.[38, 39, 40, 41, 42, 43, 44, 12, 30, 45, 46]

The central obstacle is therefore scientific rather than procedural. Melt temperature, time spent at high temperature, cooling rate, system size, and numerical controls are often chosen by convention or by computational convenience rather than by explicit criteria.[31, 33, 45, 46] Individual checks for cooling-rate sensitivity, finite-size effects, liquid stability, and ensemble variation are established in parts of the glass-simulation literature, but they

are rarely coupled into a single decision chain. Yet these choices determine whether crystalline memory is erased, whether the high-temperature liquid is sampled stably, and whether apparent structural differences are physical or numerical. Thermostat/barostat choices and neighbour-list handling are known more generally to affect simulated dynamics and, when poorly controlled, to introduce artefacts.[47, 48, 49, 50, 51, 52, 53, 54] Consequently, an apparently improved amorphous structure may reflect a better interaction model, but it may also reflect a higher melt temperature, a longer liquid hold, a slower quench, a larger cell, a different screen, or more stable numerical integration.

Workflow and provenance frameworks such as AiiDA, FireWorks, atomate, signac, and pyiron have substantially improved reproducibility of execution by standardising automation, recording data lineage, and managing heterogeneous simulation backends.[55, 56, 57, 58, 59, 60] Executional reproducibility is vital, but it does not establish structural reproducibility.[54] A workflow can preserve an under-melted liquid, an insufficient liquid hold, an over-fast quench, a numerically unstable setup, or a cell too small to support the medium-range order of interest as faithfully as it preserves a calibrated protocol. The missing layer is therefore a decision framework that tests whether the numerical setup, thermal protocol, generated structures, and resulting ensemble are adequate for the materials question being posed.

Here we introduce `Vitriflow`, a stability-constrained and convergence-aware melt–quench calibration framework for amorphous materials modelling. The methodology couples four operations that are usually treated independently or left implicit: numerical stability; systematic selection of melt temperature, liquid-hold time, quench rate, and cell size; user-defined artefact screening; and statistical convergence of the resulting ensemble in a material-specific descriptor space. Stage-resolved analysis of density, diffusion, coordination, pair structure, angular distributions, and ring or topological metrics is then used diagnostically to identify where protocol-dependent features enter the trajectory and whether they persist into the final amorphous structure.

We demonstrate this framework on three chemically distinct amorphous systems selected to exercise distinct structural-control problems. The choices reflect recurring modelling questions in functional oxides and nitrides, where local topology and defect motifs govern interfacial oxygen-ion migration, charge trapping, hydrogen response, oxidation, and charge-induced network transformation.[18, 61, 62, 63, 64, 65, 66, 67, 68] Amorphous SiO_2 tests

tetrahedral network fidelity by separating defect-free silica from oxygen-bridge-defective structures.[10, 31, 37] Amorphous Si_3N_4 tests multi-fidelity DFT refinement: a common MG2-generated structural population is relaxed at the PBE and HSE06 levels and analysed in the same descriptor space.[41, 38, 39] Amorphous Sm_2O_3 tests amorphous/crystal discrimination in a mixed-coordination rare-earth oxide, where imposing a fixed coordination rule would remove physically relevant disorder.[69, 8, 9] Together, these benchmarks establish `Vitriflow` as a computational materials methodology for turning melt–quench from a recipe for generating structures into a decision process for producing structurally controlled, statistically defensible amorphous ensembles.

2. Methodological framework

The `Vitriflow` decision sequence is shown in Fig. 1. It starts from a material-specific structural question and uses that question to define the descriptor basis, numerical stability tests, protocol-calibration criteria, artefact screens, screen actions, and analysis-ensemble convergence target.

2.1. Material problems and descriptor basis

Amorphous SiO_2, generated from β-cristobalite and treated with the SHIK-1 potential[37], tests tetrahedral network fidelity by separating defect-free silica from oxygen-bridge-defective structures. Amorphous Si_3N_4 tests controlled multi-fidelity refinement: MG2 provides the empirical melt–quench population, and PBE and HSE06 provide cell-optimised refinements of that common structural population[41]. Amorphous Sm_2O_3 tests amorphous/crystal discrimination in a charged mixed-coordination rare-earth oxide, where fixed-coordination filtering would remove physically relevant local disorder.

The framework is descriptor-driven. For a generated structure or trajectory segment x, the user specifies a descriptor map

$$\Phi(x; \mathcal{D}) = (d_1(x), d_2(x), \ldots, d_p(x)) \,, \tag{1}$$

where $\mathcal{D}$ is the material-specific descriptor set. In the present benchmarks, $\mathcal{D}$ includes density ρ, total and partial radial distribution functions $g_{\alpha\beta}(r)$, first-shell coordination numbers $n_{\alpha\beta}$, characteristic bond-angle distributions, and medium-range descriptors chosen to respect the chemistry of each network.

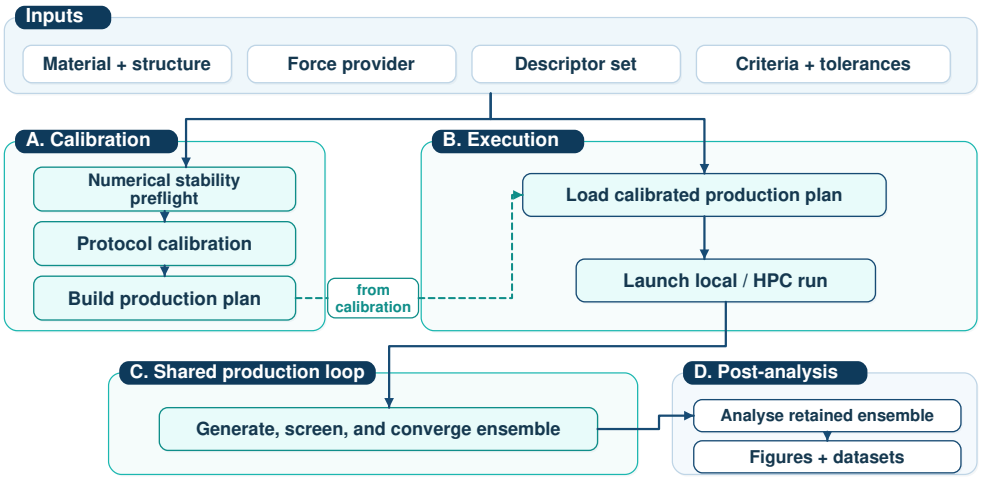

Figure 1: Overview of the `Vitriflow` decision sequence. User-defined material, structure, force provider, descriptor set, screening criteria, and convergence tolerances define both calibration and execution. The workflow first identifies numerically stable simulation settings, then calibrates the melt–hold–quench protocol and production plan, executes the shared production loop, and finally analyses the post-action ensemble. Within the production loop, generated structures receive configured screen labels, the associated `exclude` actions define the analysis ensemble, and that ensemble is expanded until the specified statistical-convergence conditions are met.

Projected Si-ring statistics are used for SiO_2, bond-graph ring statistics are used for Si_3N_4[13], and unconstrained coordination distributions and local-order metrics are used for Sm_2O_3[70, 71]. Secondary diagnostics, including $S(q)$, void-clearance distributions, and elastic or stress fingerprints, are reserved for resolving discrepancies not decided by the primary descriptor set.

2.2. Numerical stability

Before physical protocol selection, `Vitriflow` identifies the region of numerically admissible MD settings. Let

$$\theta = (\Delta t, \tau_T, \tau_P, s_n, \mathcal{C}_{\mathrm{core}}) \tag{2}$$

denote the time step, thermostat damping time, barostat damping time, neighbour skin, and any optional short-range core regularisation. For each candidate θ and each probe temperature $T^* \in \mathcal{T}_{\mathrm{probe}}$, short trajectories are run and tail statistics are evaluated. Here, $\langle\cdot\rangle_{\mathrm{tail}}$ denotes an average over

the final, post-transient portion of the short trajectory. The dimensionless temperature-control error is

$$\epsilon_T(\theta, T^*) = \frac{|\langle T \rangle_{\text{tail}} - T^*|}{T_{\text{scale}}}, \qquad T_{\text{scale}} = \max(T^*, T_{\text{floor}}), \tag{3}$$

with $T_{\text{floor}} = 1$ K used only to avoid singular scaling near zero temperature. The pressure-control error and volume sanity factor are

$$\epsilon_P(\theta, T^*) = \frac{|\langle P \rangle_{\text{tail}} - P_{\text{target}}|}{P_{\text{tol}}}, \qquad R_V(\theta, T^*) = \max\left(\frac{\langle V \rangle_{\text{tail}}}{V_{\text{ref}}}, \frac{V_{\text{ref}}}{\langle V \rangle_{\text{tail}}} \right), \tag{4}$$

where P_{target} is the applied pressure target and V_{ref} is the reference volume used to detect large box changes. For positive volumes, $R_V \geq 1$ by construction. A candidate is numerically admissible only if all hard bounds are satisfied:

$$\begin{aligned} \Theta_{\text{adm}} = \Big\{ \theta : \; & \epsilon_T(\theta, T^*) \leq \epsilon_{T,\max}, \\ & \epsilon_P(\theta, T^*) \leq \epsilon_{P,\max}, \\ & R_V(\theta, T^*) \leq R_{V,\max}, \\ & \text{for all } T^* \in \mathcal{T}_{\text{probe}}, \\ & \text{and no force, neighbour-list,} \\ & \text{or thermodynamic failure occurs} \Big\}. \end{aligned} \tag{5}$$

Surviving candidates are ranked by

$$S_{\text{pf}}(\theta) = \max_{T^* \in \mathcal{T}_{\text{probe}}} \left[\epsilon_T(\theta, T^*) + \epsilon_P(\theta, T^*) + \frac{R_V(\theta, T^*) - 1}{R_{V,\max} - 1} \right]. \tag{6}$$

The selected numerical setting $\theta^\star$ is the lowest-scoring admissible candidate, with conservative barostat damping preferred when scores are statistically indistinguishable. For Buckingham systems, the optional core $\mathcal{C}_{\text{core}}$ is treated as part of numerical admissibility and is calibrated before production tuning. Subsequent melt–quench calibration is restricted to Θ_{adm}.

2.3. Systematic protocol calibration

For an admissible numerical setting $\theta^\star$, the thermal protocol is written

$$p = (T_{\text{high}}, t_{\text{melt}}, \dot{T}, N), \tag{7}$$

where T_{high} is the high-temperature state point, t_{melt} is the liquid-hold time, $\dot{T}$ is the cooling-rate magnitude, and N is the cell size. `Vitriflow` selects the least expensive protocol, with computational cost $J(p)$, satisfying disordering, hold-time, quench-rate, and finite-size criteria:

$$p^{\star} = \arg\min_{p \in \mathcal{P}(\theta^{\star})} J(p) \quad \text{subject to} \quad \mathcal{G}_{\mathrm{melt}}, \mathcal{G}_{\mathrm{hold}}, \mathcal{G}_{\mathrm{quench}}, \mathcal{G}_{\mathrm{size}}. \tag{8}$$

The liquid-onset window, distinct from the liquid-hold time t_{melt}, is identified from a temperature ladder $T_1 < \cdots < T_M$. At each temperature, diffusion and first-peak radial-distribution descriptors define scalar transformed descriptors

$$Y_D(T) = \log(D{+}\varepsilon_D), \qquad Y_H(T) = -\log(H{+}\varepsilon_H), \qquad Y_W(T) = \log(W{+}\varepsilon_W), \tag{9}$$

where D is the diffusion estimate, H is the first-peak height, W is the first-peak width, and $\varepsilon_D, \varepsilon_H, \varepsilon_W > 0$ are small numerical floors that prevent undefined logarithms when a descriptor is zero or numerically negligible. A transition score is formed from standardised temperature derivatives,

$$\Sigma(T_i) = w_D Z[\Delta_T Y_D]_i + w_H Z[\Delta_T Y_H]_i + w_W Z[\Delta_T Y_W]_i \,, \tag{10}$$

where $Z[\cdot]$ denotes robust standardisation over the scanned temperatures. For a temperature-indexed sequence u_i,

$$Z[u]_i = \frac{u_i - \mathrm{median}(u)}{\mathrm{MAD}(u) + \varepsilon_Z}, \tag{11}$$

where MAD is the median absolute deviation and $\varepsilon_Z > 0$ prevents division by zero. The score identifies candidate transition regions, but liquid-like classification additionally requires displacement and structural gates:

$$\ell_i = \left(\frac{V_i}{N}\right)^{1/3}, \qquad \chi_i = \frac{\sqrt{\mathrm{MSD}_i}}{\ell_i}, \tag{12}$$

$$L_i = \mathbf{1}[\chi_i \geq \chi_{\star}]\, \mathbf{1}[H_i \leq \eta_H H_0]\, \mathbf{1}[W_i \geq \eta_W W_0] \,, \tag{13}$$

where H_0 and W_0 are reference first-peak descriptors, and $\chi_{\star}$, η_H, and η_W are user-set gate parameters defining the operational liquid-like state. Inactive structural gates are omitted when not required. The operational liquid onset is the first temperature in a sustained liquid-like block,

$$T_{\mathrm{liq}} = \min\{T_i : L_i = L_{i+1} = \cdots = L_{i+m-1} = 1\}, \tag{14}$$

where m is a user-configurable persistence parameter giving the number of consecutive temperature-ladder points, not MD timesteps, required for liquid-like classification. The production high-temperature set point is then

$$T_{\mathrm{high}} = T_{\mathrm{liq}} + \Delta T_{\mathrm{margin}}, \tag{15}$$

unless the user supplies a stricter material-specific bound.

At T_{high}, independent replicas determine the minimum liquid-hold time. For replica k, the disordering time is

$$t_{\mathrm{dis},k} = \inf \left\{ t \geq t_{\min} : \sqrt{\mathrm{MSD}_k(t)} \geq \alpha \ell \right\}, \tag{16}$$

subject to stationarity of density and potential energy. For a scalar thermodynamic quantity x, stationarity is assessed by

$$\delta_x = \frac{|\bar{x}_{\mathrm{late}} - \bar{x}_{\mathrm{early}}|}{\max(|\bar{x}_{\mathrm{late}}|, \varepsilon_x)}. \tag{17}$$

The assigned hold time is the worst-case disordering time across replicas,

$$t^{\star}_{\mathrm{melt}} = \max_k t_{\mathrm{dis},k}. \tag{18}$$

The cooling schedule is selected by descriptor equivalence to the slowest tested reference. For candidate rate $\dot{T}_i$ and descriptor j, let μ_{ij} and SE_{ij} be the ensemble mean and standard error, and let $\mu_{\mathrm{ref},j}$ and $\mathrm{SE}_{\mathrm{ref},j}$ denote the slow-rate reference values. Define

$$E_{ij} = |\mu_{ij} - \mu_{\mathrm{ref},j}| + c_\alpha \sqrt{\mathrm{SE}_{ij}^2 + \mathrm{SE}_{\mathrm{ref},j}^2}, \tag{19}$$

where c_α is the confidence multiplier associated with the chosen confidence level. The candidate is equivalent for descriptor j if

$$E_{ij} \leq \tau_j(\mu_{\mathrm{ref},j}), \tag{20}$$

where the descriptor-specific tolerance is

$$\tau_j(\mu) = \max(\tau_{j,\mathrm{abs}}, \tau_{j,\mathrm{rel}}|\mu|). \tag{21}$$

The absolute term prevents unrealistically tight tolerances near zero descriptor values, while the relative term scales the tolerance with descriptor magnitude; either component may be set to zero if not used. The selected quench

rate is the fastest candidate satisfying this condition for all quench-selection descriptors:

$$\dot{T}^{\star} = \max\left\{\dot{T}_i : E_{ij} \leq \tau_j(\mu_{\mathrm{ref},j})\ \forall j \in \mathcal{D}_{\mathrm{quench}}\right\}. \tag{22}$$

If no faster candidate satisfies the equivalence condition, the slowest tested rate is retained. When size scans are performed, the selected size is analogously the smallest near-cubic cell whose descriptor set is statistically indistinguishable from that of the largest tested cell.

2.4. Artefact screening and ensemble convergence

The calibrated protocol is replayed with independent random seeds to generate a population of final structures $\{x_b\}_{b=1}^{N_{\mathrm{gen}}}$. Artefact screening is optional and user-defined. A configured screen may be a single descriptor threshold or a compound rule acting on several descriptors. For screen s, the workflow evaluates the required descriptor vector

$$\mathbf{d}_{bs} = \Phi_s(x_b; \mathcal{D}_{\mathrm{screen},s}) \tag{23}$$

and stores the screen label

$$A_{bs} = \mathbf{1}[\Psi_s(\mathbf{d}_{bs}) \in \mathcal{I}_s], \tag{24}$$

where Ψ_s is the configured screen rule and $\mathcal{I}_s$ is its allowed region. Thus $A_{bs} = 1$ denotes a screen-passing cell and $A_{bs} = 0$ denotes an audit-labelled cell. If no screen is configured, no screen label is assigned.

The screen label and the analysis action are separate. Each configured screen has an `exclude` setting, $\epsilon_s = 1$ for `exclude=true` and $\epsilon_s = 0$ for `exclude=false`. The post-action analysis mask is

$$R_b = \prod_s \left[A_{bs} + (1 - A_{bs})(1 - \epsilon_s)\right], \tag{25}$$

with $R_b = 1$ when no screen is configured. The analysis ensemble is

$$\mathcal{E}_{\mathrm{ana}} = \{x_b : R_b = 1\}. \tag{26}$$

A failed screen with `exclude=true` removes the cell from analysis; a failed screen with `exclude=false` records the label but retains the cell. Numerically inadmissible settings and unresolved calibration candidates are not included in N_{gen}; $N_{A=0}$ refers only to completed final cells that receive a failing

screen label. In the present benchmarks, SiO_2 and Sm_2O_3 use `exclude=true`, whereas Si_3N_4 uses `exclude=false`.

Statistical convergence is assessed on the analysis ensemble $\mathcal{E}_{\mathrm{ana}}$. After an arbitrary but fixed ordering of analysis cells, for scalar descriptor j, the running ensemble mean after the first n analysis cells is

$$\hat{\mu}_j(n) = \frac{1}{n}\sum_{b=1}^{n} d_{bj}, \tag{27}$$

with sample variance

$$s_j^2(n) = \frac{1}{n-1}\sum_{b=1}^{n}\left(d_{bj} - \hat{\mu}_j(n)\right)^2. \tag{28}$$

The confidence half-width is

$$h_j(n) = c_{\alpha,n}\frac{s_j(n)}{\sqrt{n}}, \tag{29}$$

where $c_{\alpha,n}$ is the Student-t multiplier or its large-sample normal approximation[72]. The confidence-width ratio for descriptor j is

$$R_j(n) = \frac{h_j(n)}{\tau_j(\hat{\mu}_j(n))}, \qquad \tau_j(\mu) = \max(\tau_{j,\mathrm{abs}}, \tau_{j,\mathrm{rel}}|\mu|). \tag{30}$$

Descriptor j is converged at target q when

$$R_j(n) \le q. \tag{31}$$

For a convergence descriptor set $\mathcal{D}_{\mathrm{conv}}$, the ensemble-level convergence ratio is

$$Q(n) = \max_{j\in\mathcal{D}_{\mathrm{conv}}} R_j(n), \tag{32}$$

and the set is converged when $Q(n) \le q$. The production analyses use the default target $q_{\mathrm{conv}} = 0.2$; stricter comparison targets, such as $q = 0.1$ in Fig. 2f, are reported explicitly when used to illustrate ensemble-size sensitivity.

2.5. Stage-resolved diagnostic analysis

After protocol selection and ensemble screening, trajectory-resolved descriptors are used diagnostically to identify where protocol-dependent structural features enter. Descriptors are re-evaluated along melt, liquid-hold,

quench, and relaxation segments, with more closely spaced quench samples near the diffusion-freeze temperature T_f, defined below, where atomic mobility falls below the threshold D^*. The diffusion-freeze temperature is defined as

$$T_f = \max \{T_i : D(T_j) \leq D^* \text{ for all } T_j \leq T_i\} . \tag{33}$$

Descriptor divergence already present during the high-temperature liquid indicates incomplete loss of structural memory. Divergence arising between T_{high} and T_f identifies the quench schedule as the dominant control parameter. Divergence appearing only after cooling indicates low-temperature relaxation or residual-stress effects. Auxiliary diagnostics such as $S(q)$, void-clearance distributions, and elastic or stress fingerprints are used only when the primary descriptors do not resolve the structural origin.

3. Computational details

The workflow was executed with `Vitriflow` v0.4.27.19. Classical molecular dynamics was performed with LAMMPS[73, 74]. DFT-refinement calculations used the electronic-structure backends specified below. The main-text structural conclusions are based on the SHIK-1 a-SiO_2, MG2/PBE/HSE06 a-Si_3N_4, and Buckingham a-Sm_2O_3 datasets.

3.1. Classical molecular-dynamics setup

Classical simulations employed periodic boundary conditions and Nosé–Hoover dynamics with isotropic NPT coupling at zero target pressure[47, 48, 75, 49]. The a-SiO_2 benchmark used the SHIK-1 potential[37], a-Si_3N_4 used the MG2 potential as the empirical baseline[41], and a-Sm_2O_3 used a Coulomb–Buckingham model based on the Sm-containing oxide parameterisation of Olsson *et al.*[76, 69, 77] Time steps were selected from the admissible region identified by the stability preflight: 1.0 fs was used for a-SiO_2 and a-Si_3N_4, whereas a-Sm_2O_3 required a 0.5 fs step together with ZBL-type short-range core regularisation[78]. Temperature scans determined the operational melt window, after which liquid-hold times and quench rates were selected by the descriptor-equivalence criteria defined above. Production ensembles were generated from independent velocity seeds until the converged analysis-ensemble size was reached. Exact scan grids, hold durations, quench schedules, and stability-preflight outcomes are reported in Figs. S7, S8 and Table S2.

3.2. DFT-refined Si_3N_4 datasets

The MG2+PBE and MG2+HSE06 a-Si_3N_4 datasets were generated by cell optimisation of the MG2-derived amorphous nitride structures at the PBE and HSE06 levels, respectively. These refinements were applied to the MG2-derived structural population rather than obtained from independent DFT melt–quench trajectories.

All DFT calculations were performed spin-polarised using CP2K/ Quickstep[79, 80]. The PBE branch used the PBE exchange–correlation functional[81]; the HSE06 branch used the HSE06 hybrid functional[82, 83, 84] together with the auxiliary density matrix method (ADMM)[85] to reduce the cost of hybrid-functional exchange. DZVP-SR-MOLOPT basis sets[86] were used for valence electrons, and GTH pseudopotentials[87, 88, 89] were used for core electrons. The auxiliary plane-wave density cutoff and relative cutoff were set, after convergence testing, to 650 Ry and 70 Ry, respectively, giving an energy precision of approximately 0.1 meV atom^{-1}.

Cell optimisations were performed with the BFGS algorithm[90, 91, 92, 93]. The convergence criteria were 10^{-7} eV for energy differences and 10^{-3} eV Å^{-1} for forces. After relaxation, the same screen definitions and descriptor pipeline were applied to the MG2, MG2+PBE, and MG2+HSE06 structures.

3.3. Descriptors and comparison metrics

Descriptors were partitioned by role. The preflight and protocol-selection set comprised density, mean-squared-displacement-derived diffusion, simple radial-distribution peak descriptors, and energy stationarity. Final structural analysis was based on total and partial radial distribution functions, bond-angle distributions, coordination statistics evaluated on a fixed cutoff grid, chemically meaningful ring statistics[13], and material-specific artefact metrics. For Sm_2O_3, final comparison emphasised density, pair structure, local-order metrics[70, 71], and coordination-distribution stability rather than defect counts against a fixed allowed coordination set. Secondary diagnostics, including structure factors, void measures, and elastic or stress signatures, were retained for supporting analysis rather than for primary acceptance decisions.

Table 1: Material-specific screening outcomes. Counts are $N_{\text{gen}} : N_{A=1} : N_{A=0} : N_{\text{ana}}$, denoting generated, screen-passing, audit-labelled, and analysis cells. Hard screens use `exclude=true`; soft screens use `exclude=false`.

Material	Dataset	Screen	$N_{\text{gen}} : N_{A=1} : N_{A=0} : N_{\text{ana}}$
a-SiO_2	SHIK-1	exact coordination; hard	2533:1872:661:1872
a-Si_3N_4	MG2	coordination-outlier label; soft	455:420:35:455
a-Si_3N_4	MG2+PBE	coordination-outlier label; soft	455:451:4:455
a-Si_3N_4	MG2+HSE06	coordination-outlier label; soft	455:452:3:455
a-Sm_2O_3	Buckingham	crystal-like-order screen; hard	510:430:80:430

4. Results and discussion

Each benchmark defines a distinct structural-control problem and therefore a distinct treatment of the configured screen. In a-SiO_2, the screen tests tetrahedral network fidelity: cells that fail the exact Si:O = 4 and O:Si = 2 first-shell coordination criterion are labelled as oxygen-bridge-defective and excluded because the primary silica target is a defect-free tetrahedral network. In a-Si_3N_4, the coordination-outlier screen is configured with `exclude=false`. High-defect cells are labelled, but the full generated population is retained because residual defect content is one of the descriptors used to quantify MG2 → PBE → HSE06 refinement. In a-Sm_2O_3, the screen targets crystal-like order rather than fixed coordination; cells labelled as crystal-like are excluded because the target population is amorphous mixed-coordination Sm_2O_3. Thus the workflow applies the same sequence of screen definition, label assignment, exclude action, and ensemble convergence, while the action attached to the label is determined by the materials question.

Unless otherwise stated, uncertainties on ensemble means are reported as standard errors over the relevant analysis or audit-labelled population.

4.1. Material-specific screening and ensemble yield

Table 1 summarises the generated populations, screen labels, and analysis populations used in the main-text results. For a-SiO_2, 1872 of 2533 generated SHIK-1 cells satisfy the exact tetrahedral-network criterion, while

661 form an audited oxygen-bridge-defective comparison population. For a-Si_3N_4, the coordination-outlier screen is advisory: all 455 cells in each refinement level are used for descriptor statistics, while 35 MG2, 4 MG2+PBE, and 3 MG2+HSE06 cells carry the high-defect label. This decreasing labelled subset is part of the refinement response. The MG2 ensemble satisfies the short-, medium-, and long-range convergence groups; the PBE and HSE06 descriptors are evaluated on the MG2-derived structures relaxed at each level rather than from independently converged ensembles. For a-Sm_2O_3, the screen retains 430 of 510 generated cells as amorphous and identifies 80 cells as containing significant crystal-like character.

4.2. Tetrahedral-network fidelity in a-SiO_2

Silica provides a chemically explicit test of structural control. In an ideal continuous random network, Si is fourfold coordinated by O, and O bridges two Si atoms.[10, 16] Applying this exact first-shell criterion partitions the generated SHIK-1 population into a defect-free majority and an oxygen-bridge-defective minority (Fig. 2a). The analysis fraction is 73.9%, while 26.1% of generated cells contain at least one coordination defect. This yield demonstrates why ensemble screening is essential: a single trajectory or unfiltered average would mix two structurally distinct silica populations.

The defect population is dominated by oxygen-centred coordination errors rather than collapse of the tetrahedral Si environment. Averaged over defective cells, the Si:O selector contributes essentially no under-coordinated Si and only 0.10 over-coordinated Si centres per defective cell. The O:Si selector contributes 0.95 under-coordinated and 1.05 over-coordinated O centres per defective cell (Fig. 2b). The structural distinction is therefore specific: the excluded population primarily contains non-ideal bridging environments, while the Si-centred tetrahedral framework remains largely intact.

The two populations are close in gross structure but statistically resolved in density and local pair order. Defect-free cells have density 2.217 ± 0.001 g cm^{-3}, compared with 2.233 ± 0.002 g cm^{-3} for defective cells (Fig. 2c), in the expected range for amorphous silica.[16] The mean Si–O bond length changes weakly, from 1.6207 ± 0.00002 to 1.6210 ± 0.00004 Å, while the first Si–O peak shifts from 1.6125 ± 0.0002 to 1.6179 ± 0.0004 Å (Fig. 2d,e). The coordination screen therefore separates a chemically ideal silica ensemble from a reproducible oxygen-bridge-defective population with broader local pair structure.

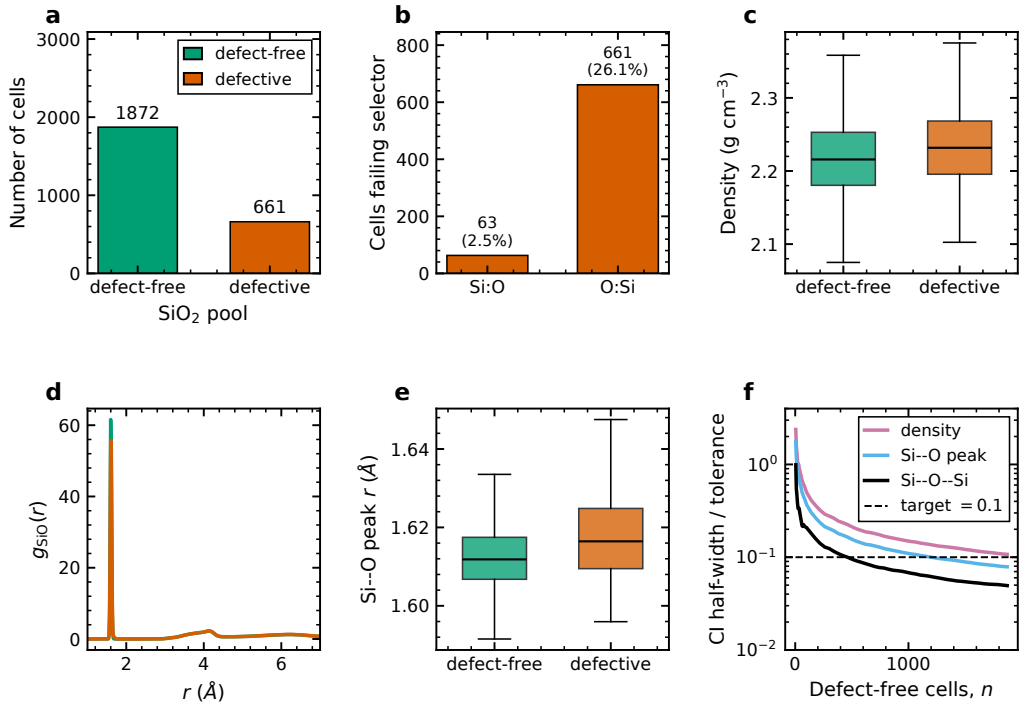

Figure 2: Coordination defects and local structure in a-SiO_2. (a) Generated-cell population partitioned into defect-free and defective silica networks using exact Si:O = 4 and O:Si = 2 first-shell coordination criteria. (b) Defective centres resolved by coordination selector, showing that the non-ideal population is dominated by oxygen-centred errors. (c) Density distributions for defect-free and defective cells. (d) Ensemble-averaged Si–O radial distribution functions over the first- and medium-range region. (e) Si–O first-peak-position distributions, showing the defect-associated shift of the first-neighbour distance. (f) Convergence of representative descriptors for the defect-free ensemble, reported as confidence half-width divided by the configured tolerance.

The defect-free silica ensemble also shows the expected relation between ensemble size and statistical precision. The production analyses use the default convergence target $q_{\mathrm{conv}} = 0.2$, for which the displayed Si–O–Si angular mean, scalar Si–O peak-height descriptor, and density reach the convergence criterion after approximately 140, 341, and 583 defect-free cells, respectively. Figure 2f plots the same confidence-width/tolerance ratios against the stricter comparison target $q = 0.1$. Under this target the angular and scalar Si–O peak-height descriptors cross after approximately 462 and 1227 cells, whereas density is the limiting displayed scalar and finishes marginally above the

threshold at $h/\tau = 0.107$ for the full defect-free ensemble of 1872 cells. Thus decreasing the target precision from 0.2 to 0.1 increases the required ensemble size substantially and shifts the limiting descriptor from local geometry to density. Full total and partial radial distribution functions, angular distributions, full-range projected Si-ring statistics, and threshold-sensitivity tests are reported in Figs. S1 and S2.

4.3. DFT-refinement hierarchy in a-Si_3N_4

The a-Si_3N_4 benchmark tests how a heteropolar amorphous network changes across a controlled MG2 → PBE → HSE06 refinement hierarchy. The PBE and HSE06 branches are cell-optimised refinements of the MG2-derived amorphous population rather than independent DFT melt–quench ensembles, making this a controlled test of model response on a common structural starting point. The same descriptor family is evaluated across all three datasets. The comparison therefore separates model-dependent structural changes from changes in the audit-label definition.

The coordination-outlier screen is configured with `exclude=false`. All 455 cells in each refinement level are therefore included in the primary descriptor statistics, while cells failing the screen remain recorded as an audit-labelled subset. This subset decreases from 35 cells for MG2 to 4 for PBE and 3 for HSE06, making the label itself a refinement-response diagnostic (Fig. 3a). Within the full analysis population, the Si:N and N:Si defect fractions are 0.0928 ± 0.0017 and 0.1441 ± 0.0015 for MG2, 0.0563 ± 0.0010 and 0.0808 ± 0.0010 for PBE, and 0.0547 ± 0.0010 and 0.0808 ± 0.0010 for HSE06 (Fig. 3d).

The refinement hierarchy changes density more strongly than the first-neighbour Si–N length scale. Relative to MG2, the PBE dataset is lower in density by 2.48%, whereas HSE06 is much closer to MG2, differing by only −0.22% (Fig. 3b). The mean Si–N bond length shifts by +0.083% for PBE and −0.69% for HSE06 (Fig. S4b). The Si–N radial distribution functions show the corresponding peak-position response: the first peaks remain similar in shape but shift slightly, with maxima at 1.7447 ± 0.0002 Å for MG2, 1.7507 ± 0.0003 Å for PBE, and 1.7374 ± 0.0003 Å for HSE06 (Fig. 3c). These peak maxima correspond to relative shifts of +0.34% for PBE and −0.42% for HSE06, as summarised in Fig. 3b.

Medium-range descriptors localise the remaining model sensitivity. The mean bond-graph ring size increases from 6.316 (MG2) to 6.658 (PBE) and 6.656 (HSE06), corresponding to relative shifts of 5.41% and 5.38%, while the

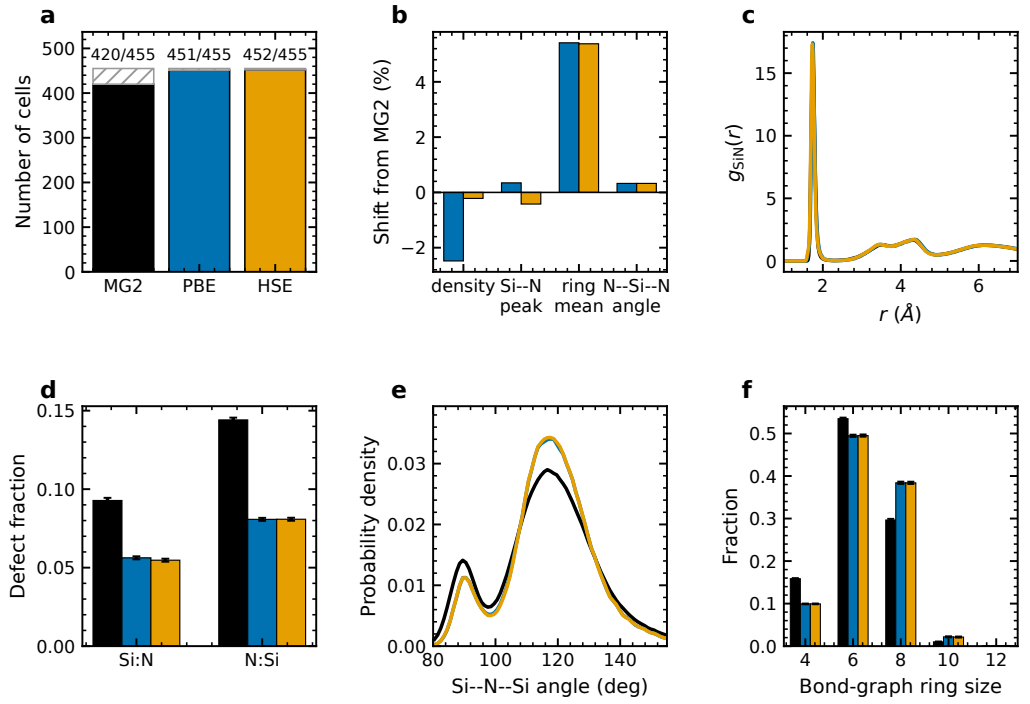

Figure 3: DFT-refinement hierarchy for a-Si_3N_4 across MG2, MG2+PBE, and MG2+HSE06 datasets. (a) Screen-passing and audit-labelled counts from the coordination-outlier screen configured with `exclude=false`; all 455 cells in each refinement level are included in the primary descriptor statistics. (b) Relative shifts in selected scalar descriptors with respect to MG2. (c) Ensemble-averaged Si–N radial distribution functions. (d) Analysis-population Si:N and N:Si coordination-defect fractions. (e) Si–N–Si angular distributions, comparing the medium-range network response across refinement levels. (f) Bond-graph ring statistics.

Si–N–Si angular mean shifts by only 0.72% and 0.75%, respectively. The full Si–N–Si angular distributions and even-member ring statistics nevertheless show a distributional network response rather than a uniform scalar offset (Fig. 3e,f). The common descriptor basis therefore resolves the refinement behaviour directly: first-shell Si–N order is comparatively robust across the hierarchy, while density, residual defect content, and cutoff-defined medium-range topology respond measurably to the model used to relax the common MG2-derived network. Complete partial radial distribution functions, $S(q)$, N–Si–N angular distributions, and scalar descriptor distributions are given in Figs. S3 and S4.

4.4. Crystal-screened mixed coordination in a-Sm_2O_3

Sm_2O_3 tests a different admissibility regime. Fixed-coordination filtering would be inappropriate because mixed Sm–O and O–Sm coordination is part of the amorphous rare-earth oxide structure.[69] The structural screen therefore targets crystal-like order. Applying the local-order criterion[70, 71] retains 430 of 510 generated structures as amorphous and assigns 80 structures to a crystal-like comparison population (Fig. 4a). The separation is large: retained cells have mean crystalline fraction 0.0257 ± 0.0015 and largest-cluster fraction 0.0232 ± 0.0014, whereas crystal-like cells have 0.348 ± 0.024 for both metrics, indicating that the crystalline atoms in these cells largely form one connected cluster (Fig. 4b).

The order metrics identify recrystallised products rather than a density tail of the amorphous distribution. Crystal-like cells occupy a higher-$\bar{q}_6$ and higher-crystalline-fraction region, while retained amorphous cells cluster below the crystalline-fraction threshold (Fig. 4c). Diffraction-derived summaries confirm the same separation, with crystal-like cells showing larger reference-peak overlap and sharper Bragg-like features (Fig. 4d). The retained ensemble also has lower density, 7.258 ± 0.004 g cm^{-3}, than the crystal-like subset, 7.368 ± 0.012 g cm^{-3}, and lower mean $\bar{q}_6$ (0.0864 ± 0.0003 versus 0.1089 ± 0.0015); the corresponding ensemble-averaged Sm–O pair correlations are shown in Fig. 4e. The screen therefore removes partially recrystallised cells while preserving the target amorphous population.

The retained Sm_2O_3 ensemble preserves mixed local coordination. Sm:O coordination is distributed mainly over five- and sixfold sites, with fractions 0.370 and 0.567, together with smaller four- and sevenfold contributions of 0.016 and 0.047. The O:Sm distribution is centred on fourfold oxygen, with fractions 0.257, 0.722, and 0.020 for three-, four-, and fivefold environments and a small twofold remainder. The mean retained coordinations are 5.646 ± 0.003 for Sm:O and 3.764 ± 0.002 for O:Sm (Fig. 4f). The material outcome is a crystal-screened amorphous rare-earth oxide ensemble with mixed coordination, not a coordination-idealised oxide network. Full $S(q)$ curves, partial pair distributions, angular descriptors, and additional scalar screening summaries are reported in Figs. S5 and S6.

4.5. Implications for computational amorphous materials modelling

The three benchmarks establish that amorphous ensemble construction is governed by material-specific structural-control problems. In SiO_2, exact coordination screening separates a statistically converged tetrahedral network

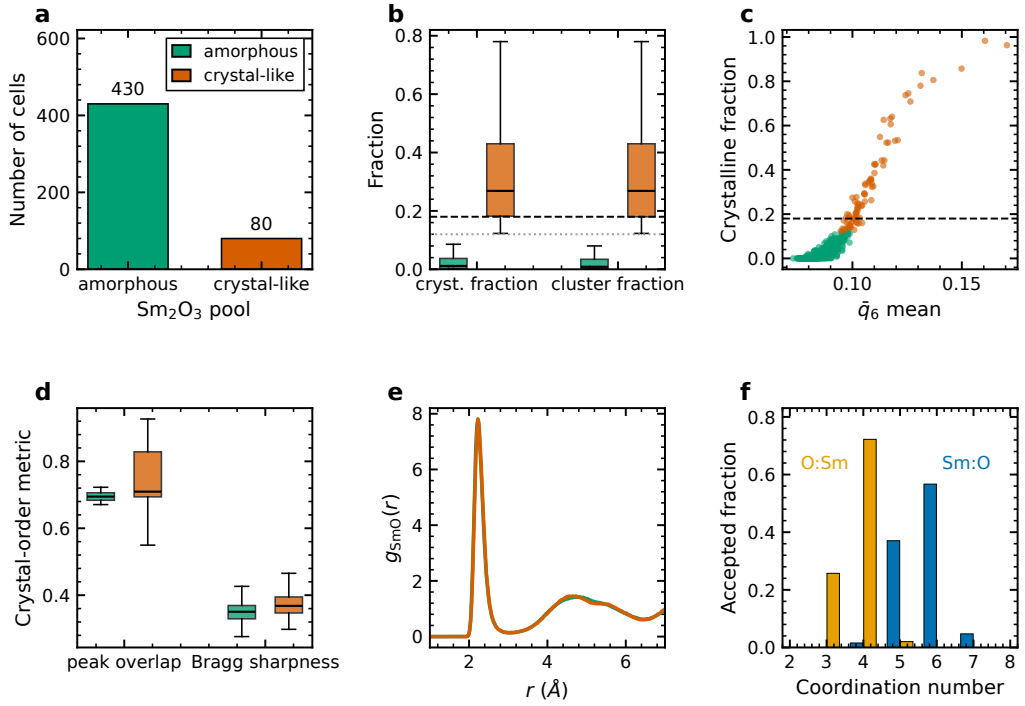

Figure 4: Amorphous/crystal discrimination and mixed coordination in a-Sm_2O_3. (a) Generated-cell population partitioned into retained amorphous and excluded crystal-like structures. (b) Crystalline-fraction and largest-cluster-fraction screening metrics, with configured thresholds shown by horizontal guides. (c) Relation between the local $\bar{q}_6$ order parameter and crystalline fraction. (d) Diffraction-derived order summaries, quantifying residual reference-peak overlap and Bragg sharpness. (e) Ensemble-averaged Sm–O radial distribution functions for retained and crystal-like structures. (f) Retained-ensemble Sm:O and O:Sm coordination-number distributions, showing that crystal screening preserves mixed local coordination.

ensemble from an oxygen-bridge-defective comparison population. In Si_3N_4, a common descriptor basis resolves how MG2-generated networks and their PBE- and HSE06-relaxed counterparts differ under refinement, with first-shell Si–N order remaining comparatively robust while density, residual defect content, and cutoff-defined medium-range descriptors respond to the energy model on a shared MG2-derived topology. In Sm_2O_3, crystal-like cells are removed without imposing a fixed coordination rule, preserving the mixed local environments required for an amorphous rare-earth oxide.

These results demonstrate the role of the full `Vitriflow` decision chain.

Stability testing and protocol calibration define the generation conditions; material-specific screening records the relevant labels and applies the configured screen actions; and statistical convergence determines whether the post-action analysis ensemble supports the reported descriptor-level comparisons. Reproducible execution alone is therefore insufficient for reproducible amorphous-structure conclusions. The required object is a calibrated, artefact-screened, statistically converged ensemble whose screening logic and descriptor precision are defined by the materials problem.

5. Conclusions

In this work, we introduced `Vitriflow`, a melt–quench calibration framework that treats amorphous model generation as a sequence of explicit computational materials decisions rather than as a fixed thermal recipe. The framework couples numerical stability preflight, systematic selection of melt temperature, liquid-hold time, quench rate and cell size, material-defined artefact screening with explicit screen actions, and statistical convergence of the post-action analysis ensemble in a prescribed descriptor space. This approach provides an audited ensemble with specified protocol parameters, screen labels, analysis population, and confidence-controlled descriptor precision.

The benchmarks show that the same decision chain resolves distinct materials problems. For a-SiO_2, exact Si:O = 4 and O:Si = 2 coordination screening retained 1872 of 2533 SHIK-1 cells and separated a statistically converged defect-free silica ensemble from an oxygen-bridge-defective comparison population. For a-Si_3N_4, all 455 generated cells in each refinement level were kept in the descriptor analysis, while the high-defect subset was recorded as an audit label. This common MG2-derived population enabled MG2, MG2+PBE, and MG2+HSE06 structures to be compared as a DFT-refinement hierarchy, showing robust first-shell Si–N order but model-sensitive density, residual defect content, and medium-range topology. For a-Sm_2O_3, local-order screening retained 430 of 510 cells as amorphous and removed crystal-like products while preserving the broad Sm–O and O–Sm coordination distributions characteristic of the mixed-coordination rare-earth oxide.

These results establish that reproducibility in amorphous modelling cannot be reduced to reproducible execution. A recorded workflow can faithfully reproduce an under-melted liquid, an over-fast quench, a numerically unstable setup, or an unfiltered ensemble containing structurally distinct products.

`Vitriflow` addresses this missing layer by selecting the numerical setup, thermal protocol, screen action, analysis population, and ensemble size against the descriptors required by the materials question. This approach defines whether the resulting amorphous ensemble is structurally controlled and statistically precise enough to support interpretation.

The framework does not replace the need for physically appropriate forces or validation against experimental observables where such data are available. Its role is more specific: it establishes whether a chosen force provider and melt–quench route produce a stable, calibrated, artefact-screened, and statistically converged ensemble for the stated structural problem. This makes amorphous model construction auditable and comparable across interaction models, electronic-structure levels, and material classes, and provides a practical standard for reporting melt–quench simulations in computational materials studies.

CRediT authorship contribution statement

Jonathon Cottom: Conceptualization, Methodology, Software, Validation, Formal analysis, Investigation, Data curation, Visualization, Writing – original draft, Writing – review & editing. **Robin Delhomme:** Methodology, Software, Validation, Formal analysis, Investigation, Data curation, Visualization, Writing – review & editing. **Emilia Olsson:** Conceptualization, Methodology, Software, Resources, Supervision, Project administration, Funding acquisition, Writing – review & editing.

Acknowledgements

The authors would like to thank Marsal Colitt Marull , Lina-Henriette Schwering and all members of the Olsson Materials Theory and Modelling group whose assistance has been invaluable in testing and refining `Vitriflow`. This work was conducted at the Advanced Research Center for Nanolithography, a public-private partnership between the University of Amsterdam (UvA), Vrije Universiteit Amsterdam (VU), Rijksuniversiteit Groningen (RUG), the Netherlands Organization for Scientific Research (NWO), and the semiconductor equipment manufacturer ASML. This work made use of the Dutch national e-infrastructure with the support of the SURF Cooperative using grant no. EINF-16595 and EINF-8981. The authors thank SURF (www.surf.nl) for the support in using the National

Supercomputer Snellius. This work made use of the ARCNL Minerva cluster hosted at HOPSTER at UvA. E.O. is grateful for a WISE Fellowship from the NWO and acknowledges support via Holland High Tech through a public-private partnership in research and development within the Dutch top sector of High-Tech Systems and Materials (HTSM).

Data availability

The `Vitriflow` package is hosted on GitHub (`https://github.com/Olsson-Materials-Modelling/Vitriflow`); the version specific to this paper is archived in the Zenodo repository [10.5281/zenodo.21111823]. The structures and post-analysis JSON files are freely available in the same Zenodo repository [10.5281/zenodo.21111823].

Declaration of competing interest

The authors declare that they have no known competing financial interests or personal relationships that could have appeared to influence the work reported in this paper.

References

[1] G. D. Wilk, R. M. Wallace, J. M. Anthony, High-κ gate dielectrics: Current status and materials properties considerations, Journal of Applied Physics 89 (10) (2001) 5243–5275. doi:10.1063/1.1361065.

[2] J. Robertson, High dielectric constant gate oxides for metal oxide Si transistors, Reports on Progress in Physics 69 (2) (2006) 327–396. doi:10.1088/0034-4885/69/2/R02.

[3] T. Kamiya, H. Hosono, Material characteristics and applications of transparent amorphous oxide semiconductors, NPG Asia Materials 2 (2010) 15–22. doi:10.1038/asiamat.2010.5.

[4] K. Nomura, H. Ohta, A. Takagi, T. Kamiya, M. Hirano, H. Hosono, Room-temperature fabrication of transparent flexible thin-film transistors using amorphous oxide semiconductors, Nature 432 (7016) (2004) 488–492. doi:10.1038/nature03090.

[5] C. Xiang, W. Jin, J. E. Bowers, Silicon nitride passive and active photonic integrated circuits: Trends and prospects, Photonics Research 10 (6) (2022) A82–A96. doi:10.1364/PRJ.452936.

[6] B. K. Yen, R. L. White, R. J. Waltman, Q. Dai, D. C. Miller, A. J. Kellock, B. Marchon, P. H. Kasai, M. F. Toney, B. R. York, H. Deng, Q.-F. Xiao, V. Raman, Microstructure and properties of ultrathin amorphous silicon nitride protective coating, Journal of Vacuum Science & Technology A 21 (6) (2003) 1895–1904. doi:10.1116/1.1615974.

[7] T. D. Lee, A. U. Ebong, A review of thin film solar cell technologies and challenges, Renewable and Sustainable Energy Reviews 70 (2017) 1286–1297. doi:10.1016/j.rser.2016.12.028.

[8] M. Leskelä, M. Ritala, Rare-earth oxide thin films as gate oxides in MOSFET transistors, Journal of Solid State Chemistry 171 (1–2) (2003) 170–174. doi:10.1016/S0022-4596(02)00204-9.

[9] A. A. Dakhel, Dielectric and optical properties of samarium oxide thin films, Journal of Alloys and Compounds 365 (1–2) (2004) 233–239. doi:10.1016/S0925-8388(03)00615-7.

[10] W. H. Zachariasen, The atomic arrangement in glass, Journal of the American Chemical Society 54 (10) (1932) 3841–3851. doi:10.1021/ja01349a006.

[11] S. R. Elliott, Medium-range structural order in covalent amorphous solids, Nature 354 (6353) (1991) 445–452. doi:10.1038/354445a0.

[12] F. Wooten, K. Winer, D. Weaire, Computer generation of structural models of amorphous Si and Ge, Physical Review Letters 54 (13) (1985) 1392–1395. doi:10.1103/PhysRevLett.54.1392.

[13] D. S. Franzblau, Computation of ring statistics for network models of solids, Physical Review B 44 (10) (1991) 4925–4930. doi:10.1103/PhysRevB.44.4925.

[14] H. E. Fischer, A. C. Barnes, P. S. Salmon, Neutron and x-ray diffraction studies of liquids and glasses, Reports on Progress in Physics 69 (1) (2006) 233–299. doi:10.1088/0034-4885/69/1/R05.

[15] P. S. Salmon, Real space manifestation of the first sharp diffraction peak in the structure factor of liquid and glassy materials, Proceedings of the Royal Society of London A 445 (1924) (1994) 351–365. doi:10.1098/rspa.1994.0065.

[16] D. A. Keen, M. T. Dove, Local structures of amorphous and crystalline phases of silica, SiO_2, by neutron total scattering, Journal of Physics: Condensed Matter 11 (47) (1999) 9263–9273. doi:10.1088/0953-8984/11/47/311.

[17] A. Pedone, Properties calculations of silica-based glasses by atomistic simulations techniques: A review, The Journal of Physical Chemistry C 113 (49) (2009) 20773–20784. doi:10.1021/jp9071263.

[18] J. Cottom, A. Bochkarev, E. Olsson, K. Patel, M. Munde, J. Spitaler, M. N. Popov, M. Bosman, A. L. Shluger, Modeling of diffusion and incorporation of interstitial oxygen ions at the TiN/SiO_2 interface, ACS Applied Materials & Interfaces 11 (39) (2019) 36232–36243. doi:10.1021/acsami.9b10705.

[19] J. K. Christie, Review: understanding the properties of amorphous materials with high-performance computing methods, Philosophical Transactions of the Royal Society A: Mathematical, Physical and Engineering Sciences 381 (2250) (2023) 20220251. doi:10.1098/rsta.2022.0251.

[20] A. Madanchi, E. Azek, K. Zongo, L. K. Béland, N. Mousseau, L. Simine, Is the future of materials amorphous? challenges and opportunities in simulations of amorphous materials, ACS Physical Chemistry Au 5 (1) (2025) 3–16. doi:10.1021/acsphyschemau.4c00063.

[21] H. Liu, Z. Zhao, Q. Zhou, R. Chen, K. Yang, Z. Wang, L. Tang, M. Bauchy, Challenges and opportunities in atomistic simulations of glasses: A review, Comptes Rendus Géoscience 354 (S1) (2022) 35–77. doi:10.5802/crgeos.116.

[22] C. Massobrio, J. Du, M. Bernasconi, P. S. Salmon (Eds.), Molecular Dynamics Simulations of Disordered Materials, Vol. 215 of Springer Series in Materials Science, Springer, Cham, 2015. doi:10.1007/978-3-319-15675-0.

[23] A. C. Wright, The comparison of molecular dynamics simulations with diffraction experiments, Journal of Non-Crystalline Solids 159 (3) (1993) 264–268. doi:10.1016/0022-3093(93)90232-M.

[24] R. Car, M. Parrinello, Unified approach for molecular dynamics and density-functional theory, Physical Review Letters 55 (22) (1985) 2471–2474. doi:10.1103/PhysRevLett.55.2471.

[25] B. W. H. van Beest, G. J. Kramer, R. A. van Santen, Force fields for silicas and aluminophosphates based on ab initio calculations, Physical Review Letters 64 (16) (1990) 1955–1958. doi:10.1103/PhysRevLett.64.1955.

[26] J. Behler, M. Parrinello, Generalized neural-network representation of high-dimensional potential-energy surfaces, Physical Review Letters 98 (14) (2007) 146401. doi:10.1103/PhysRevLett.98.146401.

[27] A. P. Bartók, M. C. Payne, R. Kondor, G. Csányi, Gaussian approximation potentials: The accuracy of quantum mechanics, without the electrons, Physical Review Letters 104 (13) (2010) 136403. doi:10.1103/PhysRevLett.104.136403.

[28] J. Behler, Perspective: Machine learning potentials for atomistic simulations, The Journal of Chemical Physics 145 (17) (2016) 170901. doi:10.1063/1.4966192.

[29] O. T. Unke, S. Chmiela, H. E. Sauceda, M. Gastegger, I. Poltavsky, K. T. Schütt, A. Tkatchenko, K.-R. Müller, Machine learning force fields, Chemical Reviews 121 (16) (2021) 10142–10186. doi:10.1021/acs.chemrev.0c01111.

[30] V. L. Deringer, N. Bernstein, A. P. Bartók, M. J. Cliffe, R. N. Kerber, L. E. Marbella, C. P. Grey, S. R. Elliott, G. Csányi, Realistic atomistic structure of amorphous silicon from machine-learning-driven molecular dynamics, The Journal of Physical Chemistry Letters 9 (11) (2018) 2879–2885. doi:10.1021/acs.jpclett.8b00902.

[31] K. Vollmayr, W. Kob, K. Binder, Cooling-rate effects in amorphous silica: A computer-simulation study, Physical Review B 54 (22) (1996) 15808–15827. doi:10.1103/PhysRevB.54.15808.

[32] J. Horbach, W. Kob, Static and dynamic properties of a viscous silica melt, Physical Review B 60 (5) (1999) 3169–3181. doi:10.1103/PhysRevB.60.3169.

[33] J. M. D. Lane, Cooling rate and stress relaxation in silica melts and glasses via microsecond molecular dynamics, Physical Review E 92 (1) (2015) 012320. doi:10.1103/PhysRevE.92.012320.

[34] A. Nakano, R. K. Kalia, P. Vashishta, First sharp diffraction peak and intermediate-range order in amorphous silica: Finite-size effects in molecular dynamics simulations, Journal of Non-Crystalline Solids 171 (2) (1994) 157–163. doi:10.1016/0022-3093(94)90351-4.

[35] S. von Alfthan, A. Kuronen, K. Kaski, Realistic models of amorphous silica: A comparative study of different potentials, Physical Review B 68 (7) (2003) 073203. doi:10.1103/PhysRevB.68.073203.

[36] T. Uchino, J. D. Harrop, S. N. Taraskin, S. R. Elliott, Real and reciprocal space structural correlations contributing to the first sharp diffraction peak in silica glass, Physical Review B 71 (1) (2005) 014202. doi:10.1103/PhysRevB.71.014202.

[37] S. Sundararaman, L. Huang, S. Ispas, W. Kob, New optimization scheme to obtain interaction potentials for oxide glasses, The Journal of Chemical Physics 148 (19) (2018) 194504. doi:10.1063/1.5023707.

[38] M. Ippolito, S. Meloni, Atomistic structure of amorphous silicon nitride from classical molecular dynamics simulations, Physical Review B 83 (16) (2011) 165209. doi:10.1103/PhysRevB.83.165209.

[39] A. Dasmahapatra, P. Kroll, Modeling amorphous silicon nitride: A comparative study of empirical potentials, Computational Materials Science 148 (2018) 165–175. doi:10.1016/j.commatsci.2017.12.008.

[40] F. de Brito Mota, J. F. Justo, A. Fazzio, Structural properties of amorphous silicon nitride, Physical Review B 58 (13) (1998) 8323–8328. doi:10.1103/PhysRevB.58.8323.

[41] C. M. Marian, M. Gastreich, J. D. Gale, Empirical two-body potential for solid silicon nitride, boron nitride, and borosilazane modifications,

Physical Review B 62 (5) (2000) 3117–3124. doi:10.1103/PhysRevB.62.3117.

[42] I. Štich, R. Car, M. Parrinello, Amorphous silicon studied by ab initio molecular dynamics: Preparation, structure, and properties, Physical Review B 44 (20) (1991) 11092–11104. doi:10.1103/PhysRevB.44.11092.

[43] M. D. Kluge, J. R. Ray, Amorphous-silicon formation by rapid quenching: A molecular-dynamics study, Physical Review B 36 (8) (1987) 4234–4237. doi:10.1103/PhysRevB.36.4234.

[44] M. Ishimaru, S. Munetoh, T. Motooka, Generation of amorphous silicon structures by rapid quenching: A molecular-dynamics study, Physical Review B 56 (23) (1997) 15133–15138. doi:10.1103/PhysRevB.56.15133.

[45] W. Li, Y. Ando, Dependence of a cooling rate on structural and vibrational properties of amorphous silicon: A neural network potential-based molecular dynamics study, The Journal of Chemical Physics 151 (11) (2019) 114101. doi:10.1063/1.5114652.

[46] I. Santos, M. Aboy, L. A. Marqués, P. López, L. Pelaz, Generation of amorphous Si structurally compatible with experimental samples through the quenching process: A systematic molecular dynamics simulation study, Journal of Non-Crystalline Solids 503–504 (2019) 20–27. doi:10.1016/j.jnoncrysol.2018.09.024.

[47] S. Nosé, A unified formulation of the constant temperature molecular dynamics methods, The Journal of Chemical Physics 81 (1) (1984) 511–519. doi:10.1063/1.447334.

[48] W. G. Hoover, Canonical dynamics: Equilibrium phase-space distributions, Physical Review A 31 (3) (1985) 1695–1697. doi:10.1103/PhysRevA.31.1695.

[49] G. J. Martyna, D. J. Tobias, M. L. Klein, Constant pressure molecular dynamics algorithms, The Journal of Chemical Physics 101 (5) (1994) 4177–4189. doi:10.1063/1.467468.

[50] J. E. Basconi, M. R. Shirts, Effects of temperature control algorithms on transport properties and kinetics in molecular dynamics simulations, Journal of Chemical Theory and Computation 9 (7) (2013) 2887–2899. doi:10.1021/ct400109a.

[51] S. C. Harvey, R. K.-Z. Tan, T. E. Cheatham III, The flying ice cube: Velocity rescaling in molecular dynamics leads to violation of energy equipartition, Journal of Computational Chemistry 19 (7) (1998) 726–740. doi:10.1002/(SICI)1096-987X(199805)19:7<726::AID-JCC4>3.0.CO;2-S.

[52] E. Braun, S. M. Moosavi, B. Smit, Anomalous effects of velocity rescaling algorithms: The flying ice cube effect revisited, Journal of Chemical Theory and Computation 14 (10) (2018) 5262–5272. doi:10.1021/acs.jctc.8b00446.

[53] H. Kim, B. Fábián, G. Hummer, Neighbor list artifacts in molecular dynamics simulations, Journal of Chemical Theory and Computation 19 (23) (2023) 8919–8929. doi:10.1021/acs.jctc.3c00777.

[54] M. W. Thompson, J. B. Gilmer, R. A. Matsumoto, C. D. Quach, P. Shamaprasad, A. H. Yang, C. R. Iacovella, C. McCabe, P. T. Cummings, Towards molecular simulations that are transparent, reproducible, usable by others, and extensible (TRUE), Molecular Physics 118 (9–10) (2020) e1742938. doi:10.1080/00268976.2020.1742938.

[55] G. Pizzi, A. Cepellotti, R. Sabatini, N. Marzari, B. Kozinsky, AiiDA: Automated interactive infrastructure and database for computational science, Computational Materials Science 111 (2016) 218–230. doi:10.1016/j.commatsci.2015.09.013.

[56] M. Uhrin, S. P. Huber, J. Yu, N. Marzari, G. Pizzi, Workflows in AiiDA: Engineering a high-throughput, event-based engine for robust and modular computational workflows, Computational Materials Science 187 (2021) 110086. doi:10.1016/j.commatsci.2020.110086.

[57] A. Jain, S. P. Ong, W. Chen, B. Medasani, X. Qu, M. Kocher, M. Brafman, G. Petretto, G.-M. Rignanese, G. Hautier, D. Gunter, K. A. Persson, FireWorks: A dynamic workflow system designed for high-throughput applications, Concurrency and Computation: Practice and Experience 27 (17) (2015) 5037–5059. doi:10.1002/cpe.3505.

[58] K. Mathew, J. H. Montoya, A. Faghaninia, S. Dwarakanath, M. Aykol, H. Tang, I.-h. Chu, T. Smidt, B. Bocklund, M. Horton, J. Dagdelen, B. Wood, Z.-K. Liu, J. Neaton, S. P. Ong, K. Persson, A. Jain, Atomate: A high-level interface to generate, execute, and analyze computational materials science workflows, Computational Materials Science 139 (2017) 140–152. doi:10.1016/j.commatsci.2017.07.030.

[59] C. S. Adorf, P. M. Dodd, V. Ramasubramani, S. C. Glotzer, Simple data and workflow management with the signac framework, Computational Materials Science 146 (2018) 220–229. doi:10.1016/j.commatsci.2018.01.035.

[60] J. Janssen, S. Surendralal, Y. Lysogorskiy, M. Todorova, T. Hickel, R. Drautz, J. Neugebauer, pyiron: An integrated development environment for computational materials science, Computational Materials Science 163 (2019) 24–36. doi:10.1016/j.commatsci.2018.07.043.

[61] K. Patel, J. Cottom, A. Mehonic, W. H. Ng, A. J. Kenyon, M. Bosman, A. L. Shluger, The nature of column boundaries in micro-structured silicon oxide nanolayers, APL Materials 9 (12) (2021) 121107. doi:10.1063/5.0073349.

[62] L. Hückmann, J. Cottom, J. Meyer, Intrinsic charge trapping and reversible charge induced structural modifications in a-Si_3N_4, Advanced Physics Research 3 (2) (2024) 2300109. doi:10.1002/apxr.202300109.

[63] J. Cottom, L. Hückmann, E. Olsson, J. Meyer, From Jekyll to Hyde and beyond: Hydrogen's multifaceted role in passivation, H-induced breakdown, and charging of amorphous silicon nitride, The Journal of Physical Chemistry Letters 15 (3) (2024) 840–848. doi:10.1021/acs.jpclett.3c03376.

[64] L. Hückmann, R. Sylvia, F. Blankenvoorde, J. Cottom, J. Meyer, Mechanistic insights into the dry oxidation of amorphous silicon nitride: A DFT study, Journal of Materials Chemistry C 14 (1) (2026) 139–151. doi:10.1039/D5TC03484A.

[65] J. Cottom, L. Hückmann, J. Meyer, E. Olsson, Forged by charge: Polaron-induced matrix formation in silicon nitride conversion-type anodes for lithium-ion batteries, Journal of Materials Chemistry A 13 (40) (2025) 34260–34272. doi:10.1039/D5TA04013B.

[66] V. L. Deringer, Modelling and understanding battery materials with machine-learning-driven atomistic simulations, Journal of Physics: Energy 2 (4) (2020) 041003. doi:10.1088/2515-7655/abb011.

[67] K. Konstantinou, F. C. Mocanu, T.-H. Lee, S. R. Elliott, Revealing the intrinsic nature of the mid-gap defects in amorphous $Ge_2Sb_2Te_5$, Nature Communications 10 (1) (2019) 3065. doi:10.1038/s41467-019-10980-w.

[68] K. Konstantinou, S. R. Elliott, J. Akola, Inherent electron and hole trapping in amorphous phase-change memory materials: $Ge_2Sb_2Te_5$, Journal of Materials Chemistry C 10 (17) (2022) 6744–6753. doi:10.1039/D2TC00486K.

[69] E. Olsson, Q. Cai, J. Cottom, R. Jakobsen, A. L. Shluger, Structural, elastic, vibrational and electronic properties of amorphous Sm_2O_3 from ab initio calculations, Computational Materials Science 169 (2019) 109119. doi:10.1016/j.commatsci.2019.109119.

[70] P. J. Steinhardt, D. R. Nelson, M. Ronchetti, Bond-orientational order in liquids and glasses, Physical Review B 28 (2) (1983) 784–805. doi:10.1103/PhysRevB.28.784.

[71] W. Lechner, C. Dellago, Accurate determination of crystal structures based on averaged local bond order parameters, The Journal of Chemical Physics 129 (11) (2008) 114707. doi:10.1063/1.2977970.

[72] Student, The probable error of a mean, Biometrika 6 (1) (1908) 1–25. doi:10.1093/biomet/6.1.1.

[73] S. Plimpton, Fast parallel algorithms for short-range molecular dynamics, Journal of Computational Physics 117 (1) (1995) 1–19. doi:10.1006/jcph.1995.1039.

[74] A. P. Thompson, H. M. Aktulga, R. Berger, D. S. Bolintineanu, W. M. Brown, P. S. Crozier, P. J. in 't Veld, A. Kohlmeyer, S. G. Moore, T. D. Nguyen, R. Shan, M. J. Stevens, J. Tranchida, C. Trott, S. J. Plimpton, LAMMPS – a flexible simulation tool for particle-based materials modeling at the atomic, meso, and continuum scales, Computer Physics Communications 271 (2022) 108171. doi:10.1016/j.cpc.2021.108171.

[75] M. Parrinello, A. Rahman, Crystal structure and pair potentials: A molecular-dynamics study, Physical Review Letters 45 (14) (1980) 1196–1199. doi:10.1103/PhysRevLett.45.1196.

[76] E. Olsson, X. Aparicio-Anglès, N. H. de Leeuw, A computational study of the electronic properties, ionic conduction, and thermal expansion of $Sm_{1-x}A_xCoO_3$ and $Sm_{1-x}A_xCoO_{3-x/2}$ (A = Ba^{2+}, Ca^{2+}, Sr^{2+}, and $x = 0.25, 0.5$) as intermediate temperature SOFC cathodes, Physical Chemistry Chemical Physics 19 (2017) 13960–13969. doi:10.1039/C7CP01555K.

[77] R. A. Buckingham, The classical equation of state of gaseous helium, neon and argon, Proceedings of the Royal Society of London A 168 (933) (1938) 264–283. doi:10.1098/rspa.1938.0173.

[78] J. F. Ziegler, J. P. Biersack, U. Littmark, The Stopping and Range of Ions in Solids, Pergamon Press, New York, 1985.

[79] T. D. Kühne, M. Iannuzzi, M. Del Ben, V. V. Rybkin, P. Seewald, F. Stein, T. Laino, R. Z. Khaliullin, O. Schütt, F. Schiffmann, D. Golze, J. Wilhelm, S. Chulkov, M. H. Bani-Hashemian, V. Weber, U. Borštnik, M. Taillefumier, A. S. Jakobovits, A. Lazzaro, H. Pabst, T. Müller, R. Schade, M. Guidon, S. Andermatt, N. Holmberg, G. K. Schenter, A. Hehn, A. Bussy, F. Belleflamme, G. Tabacchi, A. Glöß, M. Lass, I. Bethune, C. J. Mundy, C. Plessl, M. Watkins, J. VandeVondele, M. Krack, J. Hutter, CP2K: An electronic structure and molecular dynamics software package – Quickstep: Efficient and accurate electronic structure calculations, The Journal of Chemical Physics 152 (19) (2020) 194103. doi:10.1063/5.0007045.

[80] J. VandeVondele, M. Krack, F. Mohamed, M. Parrinello, T. Chassaing, J. Hutter, Quickstep: Fast and accurate density functional calculations using a mixed gaussian and plane waves approach, Computer Physics Communications 167 (2) (2005) 103–128. doi:10.1016/j.cpc.2004.12.014.

[81] J. P. Perdew, K. Burke, M. Ernzerhof, Generalized gradient approximation made simple, Physical Review Letters 77 (18) (1996) 3865–3868. doi:10.1103/PhysRevLett.77.3865.

[82] J. Heyd, G. E. Scuseria, M. Ernzerhof, Hybrid functionals based on a screened coulomb potential, The Journal of Chemical Physics 118 (18) (2003) 8207–8215. doi:10.1063/1.1564060.

[83] J. Heyd, G. E. Scuseria, M. Ernzerhof, Erratum: "hybrid functionals based on a screened coulomb potential" [J. Chem. Phys. **118**, 8207 (2003)], The Journal of Chemical Physics 124 (21) (2006) 219906. doi:10.1063/1.2204597.

[84] A. V. Krukau, O. A. Vydrov, A. F. Izmaylov, G. E. Scuseria, Influence of the exchange screening parameter on the performance of screened hybrid functionals, The Journal of Chemical Physics 125 (22) (2006) 224106. doi:10.1063/1.2404663.

[85] M. Guidon, J. Hutter, J. VandeVondele, Auxiliary density matrix methods for hartree-fock exchange calculations, Journal of Chemical Theory and Computation 6 (8) (2010) 2348–2364. doi:10.1021/ct1002225.

[86] J. VandeVondele, J. Hutter, Gaussian basis sets for accurate calculations on molecular systems in gas and condensed phases, The Journal of Chemical Physics 127 (11) (2007) 114105. doi:10.1063/1.2770708.

[87] S. Goedecker, M. Teter, J. Hutter, Separable dual-space gaussian pseudopotentials, Physical Review B 54 (3) (1996) 1703–1710. doi:10.1103/PhysRevB.54.1703.

[88] C. Hartwigsen, S. Goedecker, J. Hutter, Relativistic separable dual-space gaussian pseudopotentials from H to Rn, Physical Review B 58 (7) (1998) 3641–3662. doi:10.1103/PhysRevB.58.3641.

[89] M. Krack, Pseudopotentials for H to Kr optimized for gradient-corrected exchange-correlation functionals, Theoretical Chemistry Accounts 114 (1–3) (2005) 145–152. doi:10.1007/s00214-005-0655-y.

[90] C. G. Broyden, The convergence of a class of double-rank minimization algorithms 2. the new algorithm, IMA Journal of Applied Mathematics 6 (3) (1970) 222–231. doi:10.1093/imamat/6.3.222.

[91] R. Fletcher, A new approach to variable metric algorithms, The Computer Journal 13 (3) (1970) 317–322. doi:10.1093/comjnl/13.3.317.

[92] D. Goldfarb, A family of variable-metric methods derived by variational means, Mathematics of Computation 24 (109) (1970) 23–26. doi:10.1090/S0025-5718-1970-0258249-6.

[93] D. F. Shanno, Conditioning of quasi-newton methods for function minimization, Mathematics of Computation 24 (111) (1970) 647–656. doi:10.1090/S0025-5718-1970-0274029-X.

Supplementary Information for "`Vitriflow`: calibrated amorphous structure ensembles from melt–quench simulations"

Jonathon Cottom[a,b], Robin Delhomme[a,b], Emilia Olsson[a,b,*]

[a] *Institute for Theoretical Physics, University of Amsterdam, Science Park 904, Amsterdam, 1098 XH, the Netherlands*

[b] *Advanced Research Center for Nanolithography, Science Park 106, Amsterdam, 1098 XG, the Netherlands*

1. Supplementary methodological details

1.1. Scope, ordering, and data lineage

The supplementary methodology follows the order of the main Results section. First, the common `Vitriflow` decision machinery is specified: descriptor extraction, numerical stability preflight, protocol calibration, user-defined artefact screening, and statistical convergence. The material-specific implementations are then described in the order used in the main text: a-SiO_2 as a tetrahedral-network fidelity case, a-Si_3N_4 as a controlled DFT-refinement case, and a-Sm_2O_3 as a mixed-coordination rare-earth oxide requiring amorphous/crystal discrimination.

All supplementary data are derived from the final `Vitriflow` JSON outputs generated for the main-text analysis. The source-data deposit contains the workflow configuration files, final JSON summaries, run inputs, final relaxed structures, and descriptor tables. A generated cell denotes a trajectory that completed the configured melt–quench and final relaxation sequence. Numerical failures during preflight or calibration are treated as rejected numerical settings, not as generated cells. Cells excluded by the material-specific structural screen are retained in the audit trail and, where useful, analysed as comparison populations.

For a generated final cell x_b, with cell index $b = 1, \ldots, N_{\mathrm{gen}}$, let $\mathcal{S}_{\mathrm{screen}}$ denote the configured screens. Each screen s stores a label

$$A_{bs} \in \{0, 1\}, \tag{S1}$$

where $A_{bs} = 1$ denotes a screen-passing cell and $A_{bs} = 0$ denotes an audit-labelled cell. Each configured screen also stores an exclude setting,

$$\epsilon_s = \begin{cases} 1, & \texttt{exclude=true}, \\ 0, & \texttt{exclude=false}. \end{cases} \tag{S2}$$

The post-action analysis mask is

$$R_b = \prod_{s \in \mathcal{S}_{\mathrm{screen}}} \left[A_{bs} + (1 - A_{bs})(1 - \epsilon_s) \right], \tag{S3}$$

*Corresponding author.

Email address: `k.i.e.olsson@uva.nl` (Emilia Olsson)

with $R_b = 1$ when no screen is configured. The analysis ensemble is

$$\mathcal{E}_{\text{ana}} = \{x_b : R_b = 1\}, \qquad N_{\text{ana}} = |\mathcal{E}_{\text{ana}}|. \tag{S4}$$

For each screen, the screen-passing and audit-labelled populations are

$$\mathcal{E}^{(s)}_{A=1} = \{x_b : A_{bs} = 1\}, \qquad \mathcal{E}^{(s)}_{A=0} = \{x_b : A_{bs} = 0\}. \tag{S5}$$

For `exclude=true`, audit-labelled cells are excluded from $\mathcal{E}_{\text{ana}}$. For `exclude=false`, they remain in $\mathcal{E}_{\text{ana}}$ with the label preserved. Counts are reported as $N_{\text{gen}} : N_{A=1} : N_{A=0} : N_{\text{ana}}$, matching the notation used in the main text.

1.2. Descriptor map and descriptor roles

The workflow is descriptor-driven. For a structure or trajectory segment x, `Vitriflow` evaluates a material-specific descriptor map

$$\Phi(x; \mathcal{D}) = (d_1(x), d_2(x), \ldots, d_p(x)), \tag{S6}$$

where $\mathcal{D}$ is the descriptor set selected for the materials question. Descriptor sets are partitioned by role:

$$\mathcal{D} = \mathcal{D}_{\text{pf}} \cup \mathcal{D}_{\text{cal}} \cup \mathcal{D}_{\text{screen}} \cup \mathcal{D}_{\text{conv}} \cup \mathcal{D}_{\text{report}}. \tag{S7}$$

These subsets need not be disjoint. Here, $\mathcal{D}_{\text{pf}}$ contains quantities used for numerical stability preflight, $\mathcal{D}_{\text{cal}}$ for protocol calibration, $\mathcal{D}_{\text{screen}}$ for material-specific artefact screening, $\mathcal{D}_{\text{conv}}$ for statistical convergence, and $\mathcal{D}_{\text{report}}$ for the final structural comparisons.

The core descriptor family comprises density, total and partial radial distribution functions, first-shell coordination numbers, chemically relevant bond-angle distributions, and medium-range descriptors.[1, 2] The medium-range descriptors are chosen to avoid graph-construction artefacts: projected Si-ring statistics are used for SiO_2, primitive bond-graph rings are used for Si_3N_4, and local-order metrics are used for Sm_2O_3.[3, 4, 5] Structure factors, void-clearance distributions, elastic fingerprints, and residual-stress summaries are retained as secondary diagnostics and are not used as primary acceptance criteria unless explicitly configured.

1.3. Structural descriptor extraction

For a final relaxed cell x_b with volume V_b, the mass density is

$$\rho_b = \frac{M_b}{V_b}, \tag{S8}$$

where M_b is the total cell mass. Partial radial distribution functions are evaluated on a fixed radial grid $r_k = k\Delta r$.[1] For species α and β,

$$g^{(b)}_{\alpha\beta}(r_k) = \frac{V_b}{4\pi r_k^2 \Delta r \, N^{(b)}_\alpha \left(N^{(b)}_\beta - \delta_{\alpha\beta}\right)} \sum_{i\in\alpha} \sum_{\substack{j\in\beta \\ j\neq i}} \mathbf{1}\left[|r_{ij} - r_k| < \frac{\Delta r}{2}\right], \tag{S9}$$

where r_{ij} is the minimum-image pair distance and $\delta_{\alpha\beta}$ is the Kronecker delta. Total radial distribution functions are obtained by composition-weighted sums of the corresponding partial functions.

First-shell coordination numbers are computed from fixed cutoff radii. For an atom i of species α, the number of neighbours of species β is

$$n_{i:\beta}^{(b)} = \sum_{j\in\beta} \mathbf{1}\left[r_{ij} \le r_{\alpha\beta}^{c}\right]. \tag{S10}$$

The cutoff $r_{\alpha\beta}^{c}$ is obtained from the first minimum following the primary peak in the smoothed pair-distance histogram and is then held fixed for all cells compared within a material-specific analysis. For cross-model comparisons, the same cutoff-selection rule and fixed descriptor grid are applied to each dataset before ensemble statistics are computed.

Bond-angle distributions are evaluated on the bond graph implied by the same first-shell cutoffs. For a triplet α–β–γ, where β is the central species,

$$P_{\alpha\beta\gamma}^{(b)}(\theta_k) = \frac{1}{M_{\alpha\beta\gamma}^{(b)}} \sum_{j\in\beta} \sum_{i\in\mathcal{N}_\alpha(j)} \sum_{\substack{\ell\in\mathcal{N}_\gamma(j)\\ \ell\neq i}} \mathbf{1}\left[|\theta_{ij\ell} - \theta_k| < \frac{\Delta\theta}{2}\right], \tag{S11}$$

where $\mathcal{N}_\alpha(j)$ is the set of bonded α neighbours of central atom j, $\theta_{ij\ell}$ is the angle subtended by atoms i–j–ℓ, and $M_{\alpha\beta\gamma}^{(b)}$ is the number of counted triplets after excluding self-pairs with $i = \ell$.

Ring statistics are graph-based.[3] For SiO_2, a projected Si graph is formed by connecting two Si atoms when they share a bridging O atom:

$$(i,j) \in E_{\mathrm{SiO_2}}^{(b)} \quad\Longleftrightarrow\quad i,j \in \mathrm{Si},\ i \neq j,\ \exists\, o \in \mathrm{O} : r_{io} \le r_{\mathrm{SiO}}^{c},\ r_{jo} \le r_{\mathrm{SiO}}^{c},\ n_{o:\mathrm{Si}}^{(b)} = 2. \tag{S12}$$

Projected ring statistics are then computed on this Si graph. For Si_3N_4, rings are computed directly on the bipartite Si–N bond graph,

$$(i,j) \in E_{\mathrm{Si_3N_4}}^{(b)} \quad\Longleftrightarrow\quad i \in \mathrm{Si},\ j \in \mathrm{N},\ r_{ij} \le r_{\mathrm{SiN}}^{c}. \tag{S13}$$

Projected rings are not used for Si_3N_4 because projection through threefold N centres can generate artificial short cycles. If $R_s^{(b)}$ is the number of primitive rings of size s, the reported ring fraction is

$$p_s^{(b)} = \frac{R_s^{(b)}}{\sum_{s'} R_{s'}^{(b)}}. \tag{S14}$$

1.4. Numerical stability preflight

Before physical protocol calibration, `Vitriflow` screens the numerical settings of the molecular-dynamics calculation. Let

$$\theta = (\Delta t, \tau_T, \tau_P, s_n, \mathcal{C}_{\mathrm{core}}) \tag{S15}$$

denote the time step, thermostat damping time, barostat damping time, neighbour skin, and optional short-range repulsive core.[6, 7, 8, 9] For each candidate θ and each probe temperature

$$T^* \in \mathcal{T}_{\mathrm{probe}}, \tag{S16}$$

short trajectories are run and tail averages are computed over the final fraction of the thermodynamic record.

The dimensionless temperature-control error is

$$\epsilon_T(\theta, T^*) = \frac{|\langle T \rangle_{\text{tail}} - T^*|}{T_{\text{scale}}}, \qquad T_{\text{scale}} = \max(T^*, T_{\text{floor}}), \tag{S17}$$

with $T_{\text{floor}} = 1$ K used only to avoid singular scaling near zero temperature. The pressure-control error and volume sanity factor are

$$\epsilon_P(\theta, T^*) = \frac{|\langle P \rangle_{\text{tail}} - P_{\text{target}}|}{P_{\text{tol}}}, \tag{S18}$$

and

$$R_V(\theta, T^*) = \max\left(\frac{\langle V \rangle_{\text{tail}}}{V_{\text{ref}}}, \frac{V_{\text{ref}}}{\langle V \rangle_{\text{tail}}}\right). \tag{S19}$$

Here, P_{target} is the applied pressure target, P_{tol} is the pressure tolerance, and V_{ref} is the reference volume used to detect large box changes. The admissible numerical region is

$$\begin{aligned} \Theta_{\text{adm}} = \Big\{ \theta : \; & \epsilon_T(\theta, T^*) \le \epsilon_{T,\max}, \\ & \epsilon_P(\theta, T^*) \le \epsilon_{P,\max}, \\ & R_V(\theta, T^*) \le R_{V,\max}, \\ & \text{for all } T^* \in \mathcal{T}_{\text{probe}}, \\ & \text{and no numerical failure occurs} \Big\}. \end{aligned} \tag{S20}$$

Numerical failures include force-evaluation failures, neighbour-list failures, unstable volume excursions, non-finite thermodynamic quantities, and backend-specific molecular-dynamics errors.[10]

Surviving candidates are ranked by the preflight score

$$S_{\text{pf}}(\theta) = \max_{T^* \in \mathcal{T}_{\text{probe}}} \left[\epsilon_T(\theta, T^*) + \epsilon_P(\theta, T^*) + \frac{R_V(\theta, T^*) - 1}{R_{V,\max} - 1} \right]. \tag{S21}$$

The selected numerical setting $\theta^\star$ is the lowest-scoring admissible candidate. When scores are comparable, conservative barostat damping is preferred for NPT production. Longer high-temperature verification runs are then performed at $\theta^\star$ before physical protocol calibration.

1.5. Short-range core regularisation for Buckingham systems

For Buckingham-type interactions, the attractive $-C/r^6$ term can produce unphysical short-range collapse when atoms are driven into the repulsive-core region during high-temperature dynamics.[11, 12] In such cases, `Vitriflow` treats the short-range core $\mathcal{C}_{\text{core}}$ as part of numerical admissibility rather than as a post hoc structural correction. The core is calibrated during preflight and then fixed for all subsequent production runs.

The initial outer cutoff is determined from the median nearest-neighbour distance $\tilde{r}_{\text{nn}}$:

$$r_{\text{out}}^{(0)} = \text{clip}\left(f_{\text{out}} \tilde{r}_{\text{nn}}, r_{\text{out,min}}, r_{\text{out,max}}\right), \tag{S22}$$

and the inner cutoff is

$$r_{\mathrm{in}}^{(k)} = f_{\mathrm{in}} r_{\mathrm{out}}^{(k)}. \tag{S23}$$

Failed preflight trials widen the protected region monotonically:

$$r_{\mathrm{out}}^{(k+1)} = \min\left(r_{\mathrm{out,max}}, g\, r_{\mathrm{out}}^{(k)}\right), \qquad g > 1. \tag{S24}$$

Neighbour-skin escalation is also monotonic and is invoked only when the failure mode indicates insufficient neighbour handling. Once a stable core and neighbour skin are identified, physical protocol calibration is restricted to that admissible setting.

1.6. Systematic protocol calibration

For an admissible numerical setting $\theta^\star$, the thermal protocol is written

$$p = (T_{\mathrm{high}}, t_{\mathrm{melt}}, \dot{T}, N), \tag{S25}$$

where T_{high} is the high-temperature state point, t_{melt} is the liquid-hold time, $\dot{T}$ is the magnitude of the cooling rate, and N is the number of atoms. The selected protocol is the least expensive protocol satisfying the configured disordering, hold-time, quench-rate, and finite-size criteria:

$$p^\star = \operatorname*{arg\,min}_{p \in \mathcal{P}(\theta^\star)} J(p) \quad \text{subject to} \quad \mathcal{G}_{\mathrm{melt}}, \mathcal{G}_{\mathrm{hold}}, \mathcal{G}_{\mathrm{quench}}, \mathcal{G}_{\mathrm{size}}. \tag{S26}$$

The cost function $J(p)$ is backend-dependent and may represent wall time, number of force calls, or total simulated time. The constraints are descriptor-based and are fixed before production ensemble generation.

1.6.1. Melt-window identification

A temperature scan is performed on a ladder

$$T_1 < T_2 < \cdots < T_M. \tag{S27}$$

At each T_i, replicas provide estimates of diffusion D_i, first-peak height H_i, first-peak width W_i, volume V_i, and mean-squared displacement MSD_i.[1] Representative values are taken as medians across replicas unless otherwise specified.

The transformed indicators are

$$Y_D(T_i) = \log(D_i + \varepsilon_D), \qquad Y_H(T_i) = -\log(H_i + \varepsilon_H), \qquad Y_W(T_i) = \log(W_i + \varepsilon_W). \tag{S28}$$

Finite-difference temperature derivatives are denoted by $\Delta_T Y(T_i)$. The transition score is

$$\Sigma(T_i) = w_D Z[\Delta_T Y_D]_i + w_H Z[\Delta_T Y_H]_i + w_W Z[\Delta_T Y_W]_i, \tag{S29}$$

where $Z[\cdot]$ is a robust standardisation over the scanned temperatures,

$$Z[u]_i = \frac{u_i - \mathrm{median}(u)}{\mathrm{MAD}(u) + \varepsilon_Z}. \tag{S30}$$

The score $\Sigma(T_i)$ identifies the transition region, but a point is classified as liquid-like only if it also satisfies the displacement and structural gates. Define

$$\ell_i = \left(\frac{V_i}{N}\right)^{1/3}, \qquad \chi_i = \frac{\sqrt{\mathrm{MSD}_i}}{\ell_i}. \tag{S31}$$

The displacement gate is

$$I_\chi(i) = \mathbf{1}[\chi_i \geq \chi_\star]. \tag{S32}$$

When structural gates are active,

$$I_H(i) = \mathbf{1}[H_i \leq \eta_H H_0], \qquad I_W(i) = \mathbf{1}[W_i \geq \eta_W W_0], \tag{S33}$$

where H_0 and W_0 are the corresponding low-temperature or initial-state first-peak descriptors. Inactive structural gates are set to one. The liquid-like indicator is

$$L_i = I_\chi(i) I_H(i) I_W(i). \tag{S34}$$

The operational liquid onset is the first temperature in a sustained liquid-like block:

$$T_{\mathrm{liq}} = \min\left\{T_i : L_i = L_{i+1} = \cdots = L_{i+m-1} = 1\right\}. \tag{S35}$$

The high-temperature production set point is then

$$T_{\mathrm{high}} = T_{\mathrm{liq}} + \Delta T_{\mathrm{margin}}, \tag{S36}$$

unless a stricter user-supplied material bound is imposed.

1.6.2. Liquid-hold time

At T_{high}, independent replicas determine the minimum liquid-hold time. For replica k, the disordering time is

$$t_{\mathrm{dis},k} = \inf\left\{t \geq t_{\min} : \sqrt{\mathrm{MSD}_k(t)} \geq \alpha\ell\right\}, \tag{S37}$$

subject to stationarity of density and potential energy. For a scalar thermodynamic quantity x, stationarity between early and late windows is measured by

$$\delta_x = \frac{|\bar{x}_{\mathrm{late}} - \bar{x}_{\mathrm{early}}|}{\max(|\bar{x}_{\mathrm{late}}|, \varepsilon_x)}. \tag{S38}$$

The stationarity condition is

$$\delta_\rho \leq \eta_\rho, \qquad \delta_U \leq \eta_U, \tag{S39}$$

where U is the potential energy. The assigned liquid-hold time is the worst-case disordering time across replicas:

$$t^\star_{\mathrm{melt}} = \max_k t_{\mathrm{dis},k}. \tag{S40}$$

If no finite $t_{\mathrm{dis},k}$ is found within the configured maximum hold time, the calibration is marked unresolved and the workflow either extends the hold or returns to the melt-window selection step, depending on the configured policy.

1.6.3. Quench-rate selection

Candidate cooling rates are denoted by $\dot{T}_i > 0$, with the slowest tested rate used as the reference. For candidate rate $\dot{T}_i$, the number of quench integration steps is

$$n_q(\dot{T}_i) = \left\lceil \frac{T_{\text{high}} - T_{\text{final}}}{\dot{T}_i \, \Delta t} \right\rceil . \tag{S41}$$

For scalar descriptor j, let $\hat{\mu}_{ij}$ and SE_{ij} be the candidate ensemble mean and standard error, and let $\hat{\mu}_{\text{ref},j}$ and $\text{SE}_{\text{ref},j}$ denote the slow-rate reference. The conservative equivalence error is

$$E_{ij} = |\hat{\mu}_{ij} - \hat{\mu}_{\text{ref},j}| + c_\alpha \sqrt{\text{SE}_{ij}^2 + \text{SE}_{\text{ref},j}^2}. \tag{S42}$$

The descriptor-specific tolerance is

$$\tau_j(\mu) = \max\left(\tau_{j,\text{abs}}, \tau_{j,\text{rel}}|\mu|\right). \tag{S43}$$

The candidate rate is descriptor-equivalent to the reference if

$$E_{ij} \le \tau_j(\hat{\mu}_{\text{ref},j}) \qquad \forall j \in \mathcal{D}_{\text{quench}}. \tag{S44}$$

The selected cooling rate is the fastest equivalent candidate:

$$\dot{T}^\star = \max\left\{\dot{T}_i : E_{ij} \le \tau_j(\hat{\mu}_{\text{ref},j}) \; \forall j \in \mathcal{D}_{\text{quench}}\right\}. \tag{S45}$$

If no faster candidate satisfies the equivalence condition, the slowest tested rate is retained.

1.6.4. Finite-size selection

When size scans are performed, near-cubic cells of increasing size N_s are compared against the largest tested cell N_{ref}. For descriptor j,

$$E_{sj} = |\hat{\mu}_{sj} - \hat{\mu}_{\text{ref},j}| + c_\alpha \sqrt{\text{SE}_{sj}^2 + \text{SE}_{\text{ref},j}^2}. \tag{S46}$$

The selected size is the smallest size satisfying

$$N^\star = \min\left\{N_s : E_{sj} \le \tau_j(\hat{\mu}_{\text{ref},j}) \; \forall j \in \mathcal{D}_{\text{size}}\right\}. \tag{S47}$$

If no smaller cell is equivalent to the largest tested cell, the largest cell is retained.

1.7. User-defined artefact screening

Artefact screening is optional and user-defined. The code does not distinguish between simple and compound descriptors: a screen evaluates a configured descriptor vector and records whether the result falls inside the allowed region. For screen s,

$$\mathbf{d}_{bs} = \Phi_s(x_b; \mathcal{D}_{\text{screen},s}), \tag{S48}$$

$$\mathbf{z}_{bs} = \Psi_s(\mathbf{d}_{bs}), \tag{S49}$$

and

$$A_{bs} = \mathbf{1}\left[\mathbf{z}_{bs} \in \mathcal{I}_s\right], \tag{S50}$$

where Ψ_s is the configured screen rule and $\mathcal{I}_s$ is the allowed region. The label A_{bs} is then interpreted through the screen's `exclude` action, as defined in Sec. 1.1.

A scalar screen is recovered when $\mathbf{z}_{bs}$ has one component,

$$A_{bs}^{\mathrm{scalar}} = \mathbf{1}\left[z_{bs} \in [z_s^{\min}, z_s^{\max}]\right]. \tag{S51}$$

One-sided thresholds are obtained by setting one bound to $\pm\infty$. A reference-shifted scalar screen is the equivalent form

$$A_{bs}^{\mathrm{shift}} = \mathbf{1}\left[-\eta_s^- \le z_{bs} - z_s^{\mathrm{ref}} \le \eta_s^+\right], \tag{S52}$$

which is useful for density windows, peak-position tolerances, or other descriptors evaluated relative to a reference value.

A compound screen is a joint rule on several scalar components,

$$A_{bs}^{\mathrm{comp}} = \prod_{q=1}^{Q_s} \mathbf{1}\left[z_{bsq} \in I_{sq}\right], \tag{S53}$$

equivalently $\mathbf{z}_{bs} \in \prod_q I_{sq}$. The SiO_2 coordination screen and Sm_2O_3 crystal-like-order screen are compound examples.

For coordination-based screening, the defect fraction for central species α and neighbour species β is

$$f_{\alpha:\beta}^{(b)} = \frac{1}{N_\alpha^{(b)}} \sum_{i\in\alpha} \mathbf{1}\left[n_{i:\beta}^{(b)} \notin \mathcal{A}_{\alpha:\beta}\right], \tag{S54}$$

where $\mathcal{A}_{\alpha:\beta}$ is the allowed coordination set. A coordination screen has the form

$$A_b^{\mathrm{coord}} = \prod_{\alpha:\beta} \mathbf{1}\left[f_{\alpha:\beta}^{(b)} \le \eta_{\alpha:\beta}\right]. \tag{S55}$$

Exact coordination screening is recovered by setting the relevant $\eta_{\alpha:\beta} = 0$.

For crystal-like screening, a local-order classifier assigns

$$c_i^{(b)} \in \{0, 1\}, \tag{S56}$$

where $c_i^{(b)} = 1$ denotes a crystal-like local environment. The crystalline fraction and largest crystal-like cluster fraction are

$$f_{\mathrm{cryst}}^{(b)} = \frac{1}{N_b} \sum_{i=1}^{N_b} c_i^{(b)}, \qquad f_{\mathrm{cluster}}^{(b)} = \frac{|\mathcal{C}_{\max}^{(b)}|}{N_b}. \tag{S57}$$

The corresponding compound screen is

$$A_b^{\mathrm{cryst}} = \mathbf{1}\left[f_{\mathrm{cryst}}^{(b)} \le \eta_{\mathrm{cryst}}\right] \mathbf{1}\left[f_{\mathrm{cluster}}^{(b)} \le \eta_{\mathrm{cluster}}\right]. \tag{S58}$$

1.8. Statistical summaries and convergence criteria

Statistical convergence is assessed on the post-action analysis ensemble $\mathcal{E}_{\mathrm{ana}}$ unless explicitly stated otherwise. For scalar descriptor y, the analysis-ensemble prefix mean after n cells is

$$\bar{y}_n = \frac{1}{n}\sum_{b=1}^{n} y_b, \tag{S59}$$

and the sample variance is

$$s_n^2(y) = \frac{1}{n-1}\sum_{b=1}^{n}(y_b - \bar{y}_n)^2. \tag{S60}$$

The standard error is

$$\mathrm{SE}_n(y) = \frac{s_n(y)}{\sqrt{n}}. \tag{S61}$$

The confidence half-width is

$$h_n(y) = c_{\alpha,n}\frac{s_n(y)}{\sqrt{n}}, \tag{S62}$$

where $c_{\alpha,n}$ is the Student-t multiplier $t_{1-\alpha/2,n-1}$ or its large-sample normal approximation.[13]

The descriptor-specific convergence tolerance is

$$\tau_y(\bar{y}_n) = \max\left(\tau_{y,\mathrm{abs}}, \tau_{y,\mathrm{rel}}|\bar{y}_n|\right). \tag{S63}$$

The confidence-width ratio is

$$R_y(n) = \frac{h_n(y)}{\tau_y(\bar{y}_n)}. \tag{S64}$$

Descriptor y is converged at prefix size n when

$$R_y(n) \le 0.2. \tag{S65}$$

For the convergence descriptor set $\mathcal{D}_{\mathrm{conv}}$, the ensemble-level convergence ratio is

$$Q(n) = \max_{y\in\mathcal{D}_{\mathrm{conv}}} R_y(n). \tag{S66}$$

The analysis ensemble is converged when

$$Q(n) \le 0.2. \tag{S67}$$

The confidence-width/tolerance curves shown in the main figures are plots of $R_y(n)$ or $Q(n)$.

For bounded descriptors scaled to $[0,1]$, empirical Bernstein and Hoeffding bounds are also evaluated[14, 15]:

$$h_n^{\mathrm{EB}} = \sqrt{\frac{2\hat{v}_n \ln(3/\alpha)}{n}} + \frac{3\ln(3/\alpha)}{n}, \tag{S68}$$

$$h_n^{\mathrm{H}} = \sqrt{\frac{\ln(2/\alpha)}{2n}}, \tag{S69}$$

where $\hat{v}_n$ is the empirical variance of the scaled descriptor. For descriptors originally defined on $[a,b]$, the bounds are evaluated after affine scaling to $[0,1]$ and then rescaled to the original units.

Distributional stability is monitored for fixed-grid descriptors such as radial distribution functions, angular distributions, and ring histograms. For empirical cumulative distribution functions F_A and F_B, the Wasserstein-1 distance is[16]

$$W_1(F_A, F_B) = \int_{-\infty}^{\infty} |F_A(t) - F_B(t)|\, dt, \tag{S70}$$

and the Kolmogorov–Smirnov distance is[17]

$$D_{\mathrm{KS}}(F_A, F_B) = \sup_t |F_A(t) - F_B(t)|. \tag{S71}$$

For fixed-grid histograms, the same definitions are evaluated on the common grid. Distributional tests are used to identify drift between analysis-cell prefixes, between analysis and audit-labelled populations, or between interaction-model datasets.

1.9. Stage-resolved diagnostic analysis

Stage-resolved analysis is diagnostic rather than a separate acceptance layer. For each trajectory, descriptors are evaluated along the melt, liquid-hold, quench, and relaxation segments. Let $d_j(s,t)$ denote descriptor j evaluated at time t in stage s. For two populations A and B, the normalised descriptor separation is

$$\Delta_j^{A,B}(s,t) = \frac{|\hat{\mu}_{A,j}(s,t) - \hat{\mu}_{B,j}(s,t)|}{\tau_j(\hat{\mu}_{B,j}(s,t))}. \tag{S72}$$

A divergence is considered structurally relevant when $\Delta_j^{A,B}(s,t) > 1$ and persists over the configured time or temperature window.

During cooling, the diffusion-freeze temperature is defined as

$$T_f = \max\left\{T_i : D(T_j) \le D^* \text{ for all } T_j \le T_i\right\}. \tag{S73}$$

Divergence already present in the high-temperature liquid indicates incomplete loss of structural memory. Divergence emerging between T_{high} and T_f identifies the quench schedule as the dominant control parameter. Divergence appearing only after cooling indicates low-temperature relaxation, residual-stress effects, or final minimisation effects. Secondary diagnostics such as $S(q)$, void-clearance distributions, elastic fingerprints, and residual-stress summaries are used only when the primary descriptor set does not resolve the origin of the divergence.

1.10. a-SiO_2: tetrahedral-network fidelity

The a-SiO_2 benchmark tests whether the generated amorphous silica population satisfies the chemically ideal tetrahedral network definition. The classical main-text dataset is generated from β-cristobalite-derived starting structures using the SHIK-1 potential.[18]

The primary structural screen is exact first-shell coordination. For each cell,

$$f_{\mathrm{Si:O}}^{(b)} = \frac{1}{N_{\mathrm{Si}}^{(b)}} \sum_{i \in \mathrm{Si}} \mathbf{1}\left[n_{i:\mathrm{O}}^{(b)} \neq 4\right], \tag{S74}$$

and

$$f_{\mathrm{O:Si}}^{(b)} = \frac{1}{N_{\mathrm{O}}^{(b)}} \sum_{i \in \mathrm{O}} \mathbf{1}\left[n_{i:\mathrm{Si}}^{(b)} \neq 2\right]. \tag{S75}$$

The SiO_2 coordination-screen label is

$$A_b^{\mathrm{SiO_2}} = \mathbf{1}\left[f_{\mathrm{Si:O}}^{(b)} = 0\right] \mathbf{1}\left[f_{\mathrm{O:Si}}^{(b)} = 0\right]. \tag{S76}$$

This screen is configured with `exclude=true`. Thus, $A_b^{\mathrm{SiO_2}} = 1$ cells form the defect-free silica analysis ensemble: all Si centres are fourfold coordinated by O and all O centres are twofold coordinated by Si. Cells with $A_b^{\mathrm{SiO_2}} = 0$ are excluded from the silica analysis ensemble and retained as the oxygen-bridge-defective audit population analysed in the main text.

The SiO_2 reporting descriptor set comprises density, total and partial radial distribution functions, the Si–O first-peak position and height, O–Si–O and Si–O–Si angular distributions, and projected Si-ring statistics. The convergence descriptor groups include representative scalar descriptors from the local, angular, and medium-range sets. The projected-ring graph is built only through bridging O atoms satisfying $n_{\mathrm{O:Si}} = 2$, ensuring that the ring topology describes the chemically admissible tetrahedral network rather than defect-mediated graph artefacts.

Threshold sensitivity is evaluated by recomputing the analysis fraction and key descriptor means under controlled perturbations of the first-shell cutoff grid. The final reported SiO_2 ensemble uses the fixed cutoff table archived with the source data.

1.11. a-Si_3N_4: controlled DFT refinement

The a-Si_3N_4 benchmark tests controlled multi-fidelity refinement in a heteropolar amorphous network. The MG2 dataset is the empirical melt–quench population.[19] The MG2+PBE and MG2+HSE06 datasets are PBE- and HSE06-relaxed descendants of the MG2-derived amorphous population, analysed with the same screen definitions, descriptor pipeline, and statistical workflow.[20, 21, 22, 23] The comparison is therefore a controlled refinement analysis under common descriptors, not an independent DFT melt–quench comparison or a single-score ranking of interaction models.

Nominal coordination defects are defined using

$$\mathcal{A}_{\mathrm{Si:N}} = \{4\}, \qquad \mathcal{A}_{\mathrm{N:Si}} = \{3\}. \tag{S77}$$

The corresponding defect fractions are

$$f_{\mathrm{Si:N}}^{(b)} = \frac{1}{N_{\mathrm{Si}}^{(b)}} \sum_{i \in \mathrm{Si}} \mathbf{1}\left[n_{i:\mathrm{N}}^{(b)} \notin \mathcal{A}_{\mathrm{Si:N}}\right], \tag{S78}$$

and

$$f_{\mathrm{N:Si}}^{(b)} = \frac{1}{N_{\mathrm{N}}^{(b)}} \sum_{i \in \mathrm{N}} \mathbf{1}\left[n_{i:\mathrm{Si}}^{(b)} \notin \mathcal{A}_{\mathrm{N:Si}}\right]. \tag{S79}$$

Unlike the SiO_2 case, the nitride coordination screen is not an exact zero-defect rejection condition. Residual Si:N and N:Si defect fractions are refinement-response descriptors. The configured thresholds define a coordination-outlier screen label,

$$A_b^{\mathrm{Si_3N_4}} = \mathbf{1}\left[f_{\mathrm{Si:N}}^{(b)} \leq \eta_{\mathrm{Si:N}}^{\mathrm{audit}}\right] \mathbf{1}\left[f_{\mathrm{N:Si}}^{(b)} \leq \eta_{\mathrm{N:Si}}^{\mathrm{audit}}\right]. \tag{S80}$$

This screen is configured with `exclude=false`. Therefore

$$\mathcal{E}_{\mathrm{ana}}^{\mathrm{Si_3N_4}} = \{x_b : b = 1, \ldots, N_{\mathrm{gen}}\}, \qquad \mathcal{E}_{A=0}^{\mathrm{Si_3N_4}} = \{x_b : A_b^{\mathrm{Si_3N_4}} = 0\}. \tag{S81}$$

The audit-labelled subset is reported as a refinement diagnostic, while residual defect fractions are reported over the full analysis ensemble:

$$\bar{f}_{\alpha:\beta} = \frac{1}{|\mathcal{E}_{\mathrm{ana}}|} \sum_{x_b \in \mathcal{E}_{\mathrm{ana}}} f_{\alpha:\beta}^{(b)}. \tag{S82}$$

The Si_3N_4 descriptor set comprises density, Si–N radial distribution functions, Si–N first-peak position and height, N–Si–N and Si–N–Si angular distributions, analysis-ensemble Si:N and N:Si defect fractions, and primitive rings on the bipartite Si–N graph. Because the Si–N graph is bipartite, chemically meaningful rings have even size. For model $M \in \{\mathrm{PBE}, \mathrm{HSE06}\}$, scalar shifts relative to MG2 are reported as

$$\Delta_j^M = 100 \frac{\hat{\mu}_{M,j} - \hat{\mu}_{\mathrm{MG2},j}}{\hat{\mu}_{\mathrm{MG2},j}} \ \%. \tag{S83}$$

This normalisation is used only for reporting relative shifts; convergence is assessed on the original descriptor values and tolerances.

The configured convergence groups separate short-range descriptors, medium-range descriptors, and long-range diagnostics. The short-range group includes density, Si–N first-shell pair descriptors, and coordination-defect fractions. The medium-range group includes angular and bond-graph ring descriptors. Long-range diagnostics include low-q structure-factor features or void/stress fingerprints when configured.

1.12. a-Sm_2O_3: mixed coordination and crystal-like screening

The a-Sm_2O_3 benchmark tests the stability and screening layers in a charged mixed-coordination rare-earth oxide. The classical dataset uses a Coulomb–Buckingham interaction model with the short-range core regularisation described in Sec. 1.5.[11, 12] The calibrated core is treated as part of the numerical model used to obtain stable high-temperature dynamics; it is not used as a structural acceptance criterion.

Fixed-coordination screening is not used for Sm_2O_3 because mixed Sm–O and O–Sm coordination is part of the target amorphous structure. The primary screen targets crystal-like order. For local bond-order analysis, a local spherical-harmonic descriptor may be written as[4, 5]:

$$q_{\ell m}(i) = \frac{1}{N_i} \sum_{j=1}^{N_i} Y_{\ell m}(\hat{\mathbf{r}}_{ij}), \tag{S84}$$

with rotationally invariant magnitude

$$q_\ell(i) = \left[\frac{4\pi}{2\ell+1} \sum_{m=-\ell}^{\ell} |q_{\ell m}(i)|^2 \right]^{1/2}. \tag{S85}$$

The reported local-order summary uses the configured $\bar{q}_6$ statistic. An atom is classified as crystal-like when its local-order descriptor falls inside the configured crystalline reference region:

$$c_i^{(b)} = \mathbf{1}\left[\omega(\mathbf{q}_i^{(b)}) \in I_{\mathrm{cryst}}\right], \tag{S86}$$

where ω denotes the configured local-order classifier. The crystalline fraction and largest crystal-like cluster fraction are

$$f_{\mathrm{cryst}}^{(b)} = \frac{1}{N_b} \sum_{i=1}^{N_b} c_i^{(b)}, \tag{S87}$$

and

$$f_{\mathrm{cluster}}^{(b)} = \frac{|\mathcal{C}_{\mathrm{max}}^{(b)}|}{N_b}. \tag{S88}$$

The Sm_2O_3 crystal-like-order screen label is

$$A_b^{\mathrm{Sm_2O_3}} = \mathbf{1}\left[f_{\mathrm{cryst}}^{(b)} \le \eta_{\mathrm{cryst}}\right] \mathbf{1}\left[f_{\mathrm{cluster}}^{(b)} \le \eta_{\mathrm{cluster}}\right]. \tag{S89}$$

This screen is configured with `exclude=true`. Therefore $A_b^{\mathrm{Sm_2O_3}} = 1$ cells form the retained amorphous analysis ensemble, while $A_b^{\mathrm{Sm_2O_3}} = 0$ cells form the excluded crystal-like audit population.

Diffraction-derived order summaries are used as supporting validation of the same classification. Let $\mathbf{p}^{(b)}$ be the vector of background-subtracted intensities at the configured crystalline reference peak positions, and let $\mathbf{p}^{\mathrm{ref}}$ be the corresponding reference vector. The reference-peak overlap is

$$O_{\mathrm{ref}}^{(b)} = \frac{\mathbf{p}^{(b)} \cdot \mathbf{p}^{\mathrm{ref}}}{\|\mathbf{p}^{(b)}\| \, \|\mathbf{p}^{\mathrm{ref}}\|}. \tag{S90}$$

A Bragg-sharpness score $B^{(b)}$ is evaluated from the configured peak-width or peak-prominence measure in the structure factor. These diffraction summaries are reported alongside f_{cryst} and f_{cluster} to confirm that rejected cells are crystal-like rather than merely high-density amorphous outliers.

The Sm_2O_3 reporting descriptor set comprises density, Sm–O and O–Sm coordination distributions, total and partial radial distribution functions, local-order metrics, reference-peak overlap, Bragg sharpness, and angular descriptors when required. The retained-amorphous analysis-ensemble coordination distribution for central species α and neighbour species β is

$$p_{\alpha:\beta}(m) = \frac{\sum_{x_b \in \mathcal{E}_{\mathrm{ana}}} \sum_{i \in \alpha} \mathbf{1}[n_{i:\beta}^{(b)} = m]}{\sum_{x_b \in \mathcal{E}_{\mathrm{ana}}} N_\alpha^{(b)}}. \tag{S91}$$

This distribution is reported directly, rather than compared with a fixed ideal coordination set.

1.13. Reproducibility outputs

For each benchmark, the archived `Vitriflow` output records the numerical preflight candidates, preflight scores, selected numerical setting $\theta^\star$, temperature-scan summaries, selected T_{high}, selected $t_{\mathrm{melt}}^\star$, selected cooling rate $\dot{T}^\star$, size-scan outcome when applicable, production seed list, screening functions, screening thresholds, `exclude` settings, screen labels, analysis masks, descriptor tables, convergence ratios, and figure-generation inputs. The source-data archive therefore distinguishes three classes of rejected object:

1. numerically inadmissible settings rejected during preflight;

2. unresolved protocol candidates rejected during calibration;
3. generated final cells screened by material-specific artefact screening.

Only the third class contributes to the $N_{A=0}$ audit-labelled counts reported in the main-text screening table.

2. Supplementary figures

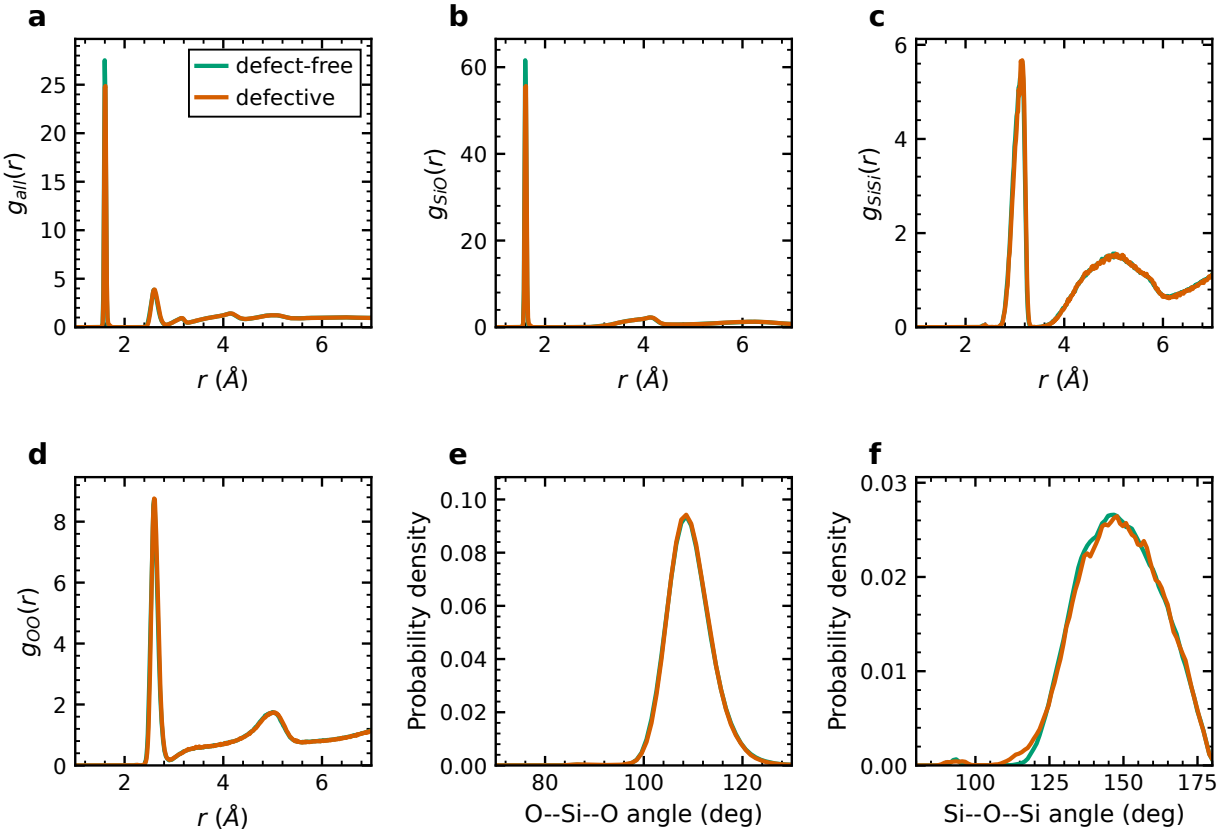

Figure S1: a-SiO_2 structural descriptors for the defect-free and defective populations. (a) Total radial distribution function. (b) Si–O partial radial distribution function. (c) Si–Si partial radial distribution function. (d) O–O partial radial distribution function. (e) O–Si–O angular distribution. (f) Si–O–Si angular distribution. Radial distribution functions are restricted to the structurally informative 1–7 Å range.

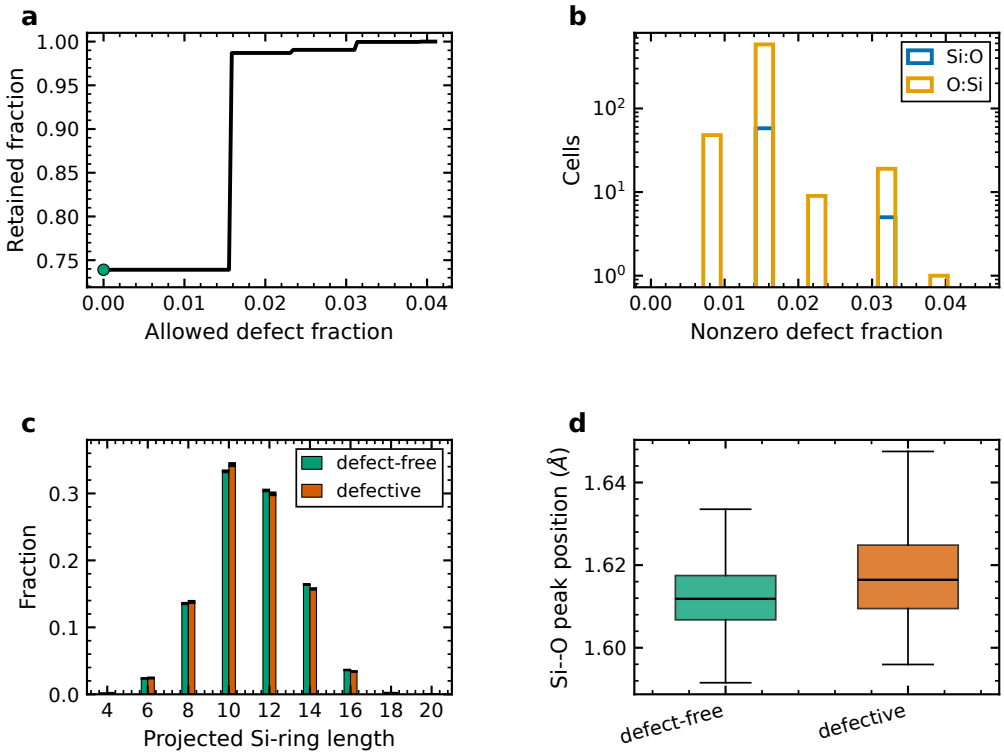

Figure S2: a-SiO_2 screening details. (a) Retained fraction as a function of the allowed maximum coordination-defect fraction. (b) Distribution of nonzero defect fractions for the Si:O and O:Si selectors. (c) Even-member projected Si-ring statistics for the defect-free and defective populations. (d) Si–O first-peak-position distributions.

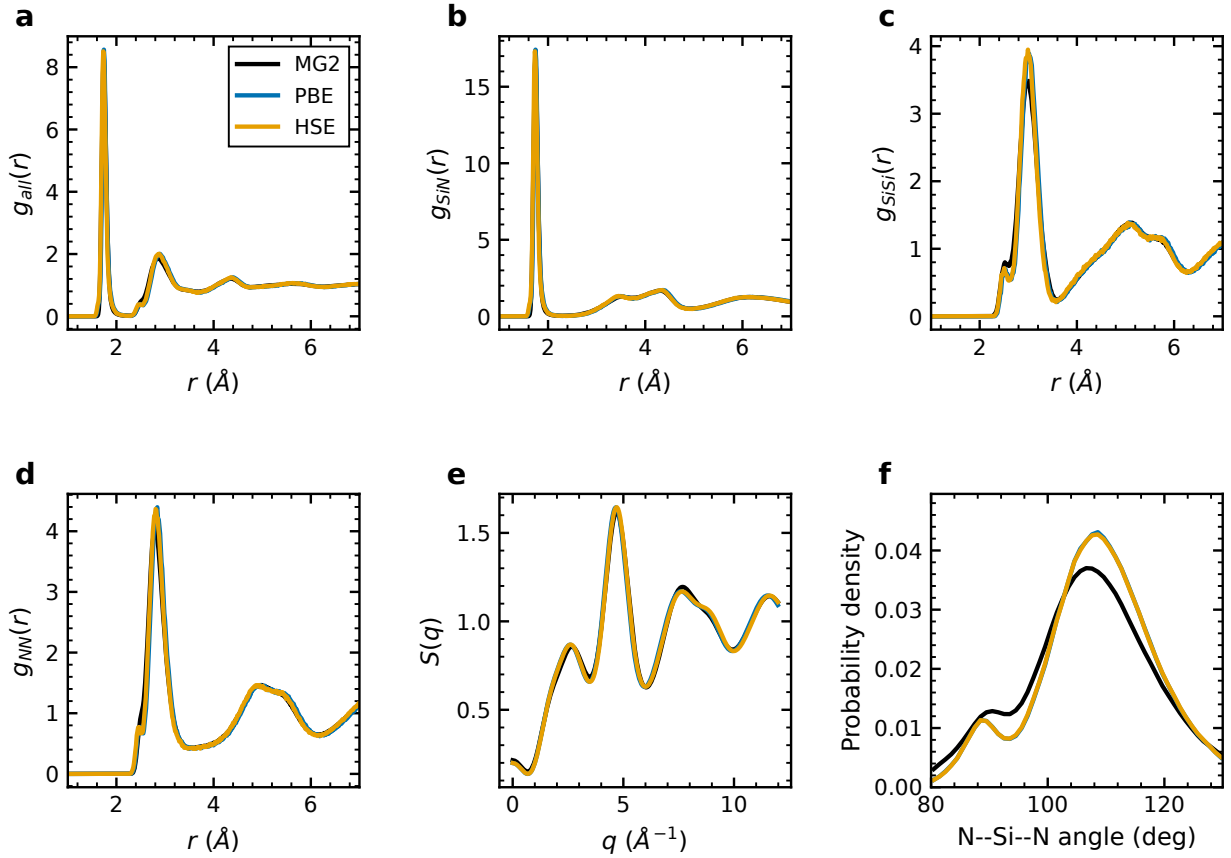

Figure S3: a-Si_3N_4 MG2/PBE/HSE06 structural comparison. (a) Total radial distribution function. (b) Si–N partial radial distribution function. (c) Si–Si partial radial distribution function. (d) N–N partial radial distribution function. (e) Total structure factor. (f) N–Si–N angular distribution. Radial distribution functions are restricted to 1–7 Å.

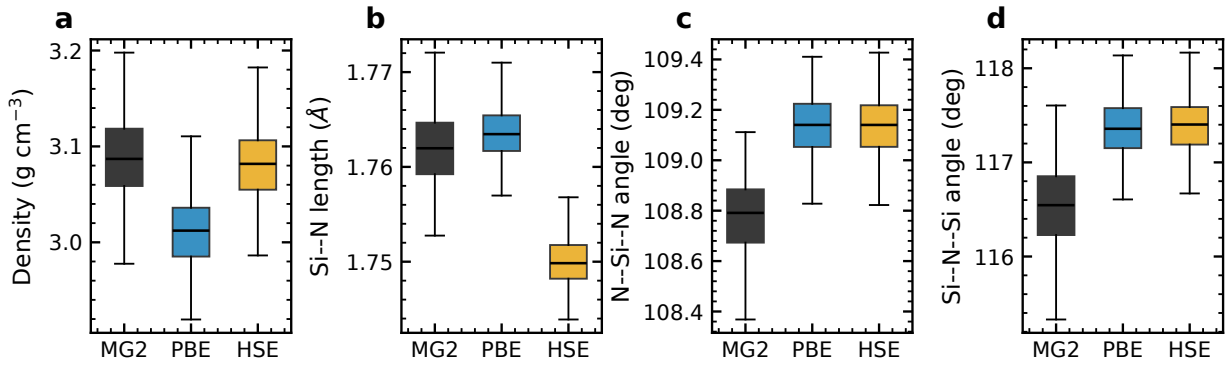

Figure S4: a-Si_3N_4 scalar descriptor distributions for the MG2, PBE, and HSE06 datasets. (a) Density. (b) Mean Si–N bond length. (c) Mean N–Si–N angle. (d) Mean Si–N–Si angle.

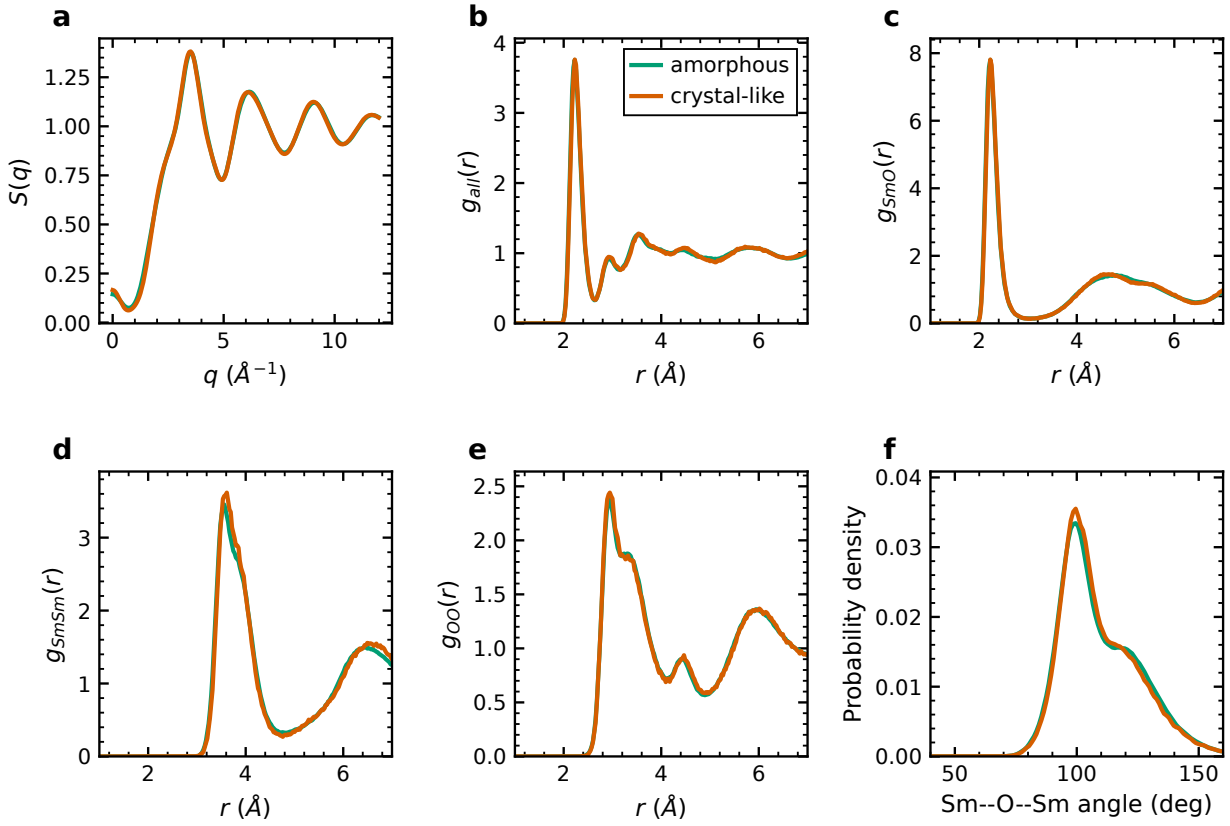

Figure S5: a-Sm_2O_3 structural descriptors for retained amorphous and excluded crystal-like cells. (a) Total structure factor. (b) Total radial distribution function. (c) Sm–O partial radial distribution function. (d) Sm–Sm partial radial distribution function. (e) O–O partial radial distribution function. (f) Sm–O–Sm angular distribution. Radial distribution functions are restricted to 1–7 Å.

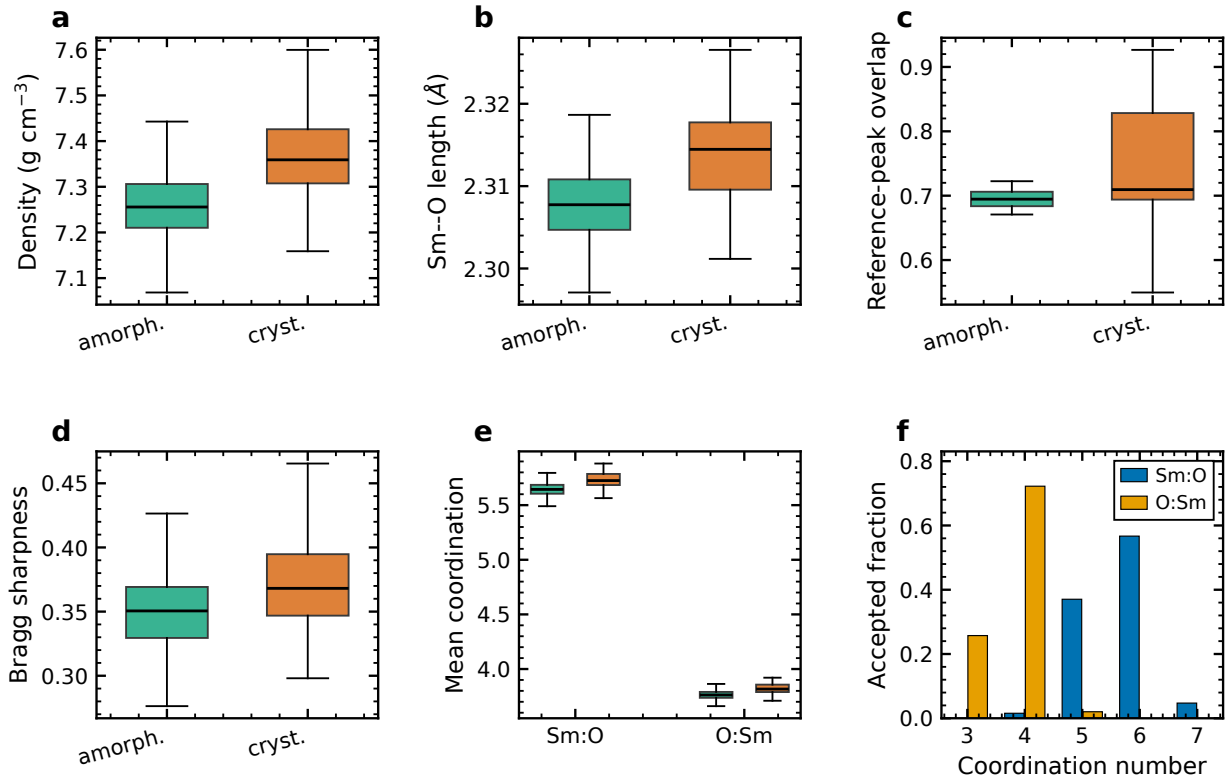

Figure S6: a-Sm_2O_3 screening descriptors for retained amorphous and excluded crystal-like cells. (a) Density. (b) Mean Sm–O bond length. (c) Reference-peak overlap. (d) Bragg sharpness. (e) Mean Sm:O and O:Sm coordination. (f) Retained amorphous fraction by coordination number for Sm:O and O:Sm environments.

3. Supplementary tables

Table S1: Generated, screen-labelled, and analysis populations for the final datasets. Counts follow the main-text notation $N_{\mathrm{gen}} : N_{A=1} : N_{A=0} : N_{\mathrm{ana}}$.

Case	Dataset	Screen	$N_{\mathrm{gen}} : N_{A=1} : N_{A=0} : N_{\mathrm{ana}}$
SiO_2	SHIK-1	exact Si:O = 4 and O:Si = 2 coordination; `exclude=true`	2533:1872:661:1872
Si_3N_4	MG2	coordination-outlier label; `exclude=false`	455:420:35:455
Si_3N_4	MG2+PBE	coordination-outlier label; `exclude=false`	455:451:4:455
Si_3N_4	MG2+HSE06	coordination-outlier label; `exclude=false`	455:452:3:455
Sm_2O_3	Buckingham	crystal-like-order screen; `exclude=true`	510:430:80:430

4. Supplementary calibration scans

The available autotune-pass figures are shown below and summarised in Table S2. Vertical markers denote the selected melt, liquid, and high-temperature set points; shaded bands are the replica standard deviation. The temperature-ladder panels (diffusion, $g(r)$ peak height and width, density, potential energy, RMS displacement) realise the melt-window logic of Sec. 1.6.1; the rate-scan panels realise the descriptor-equivalence quench selection of Sec. 1.6.3.

Table S2: Autotuned production settings for independently generated melt–quench populations. Classical runs used periodic NPT isothermal-isobaric ensemble at 0 bar.

Parameter	a-SiO_2	a-Si_3N_4	a-Sm_2O_3
model	SHIK-1	MG2	Buck.
atoms	192	280	350
Δt (fs)	1.0	1.0	0.5
τ_T/τ_P (ps)	0.5/5.0	0.50/5.0	0.05/1.0
s_n (Å)	0.25	0.5	1.0
$T_m/T_{\mathrm{liq}}/T_{\mathrm{high}}$ (K)	4000/4500/5000	2500/3500/4000	2000/3500/4000
$t^{\star}_{\mathrm{warm}}$ (ps)	5	5	5
$t^{\star}_{\mathrm{melt}}$ (ps)	50	107.8	44.0
$T^{\star}$ (K ps^{-1})	1.0	1.0	50.0
T_{final} (K); relax (ps)	300; 100	300; 100	300; 100
core	none	none	ZBL 1.100/1.375 Å

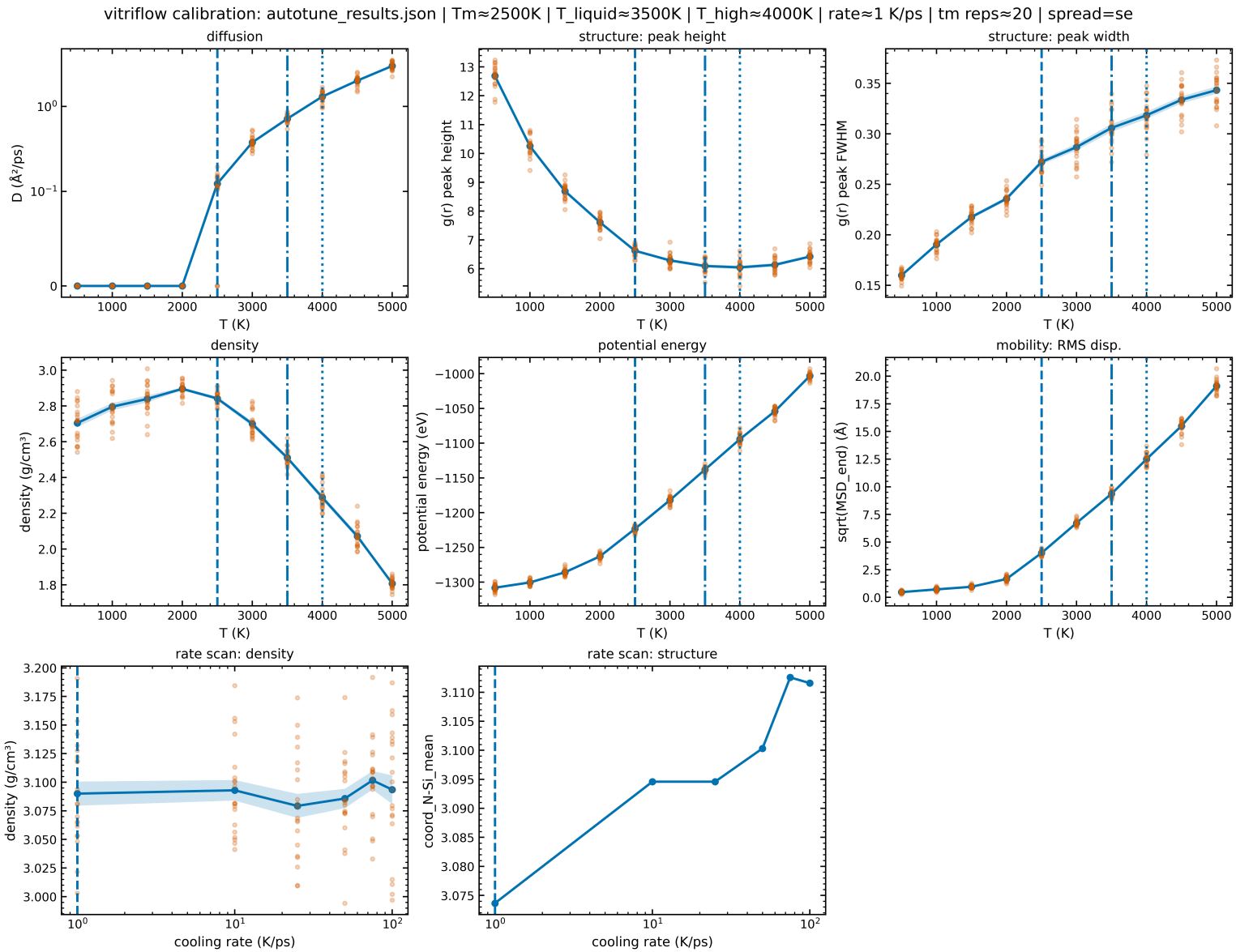

Figure S7: a-Si_3N_4 `Vitriflow` calibration scan.

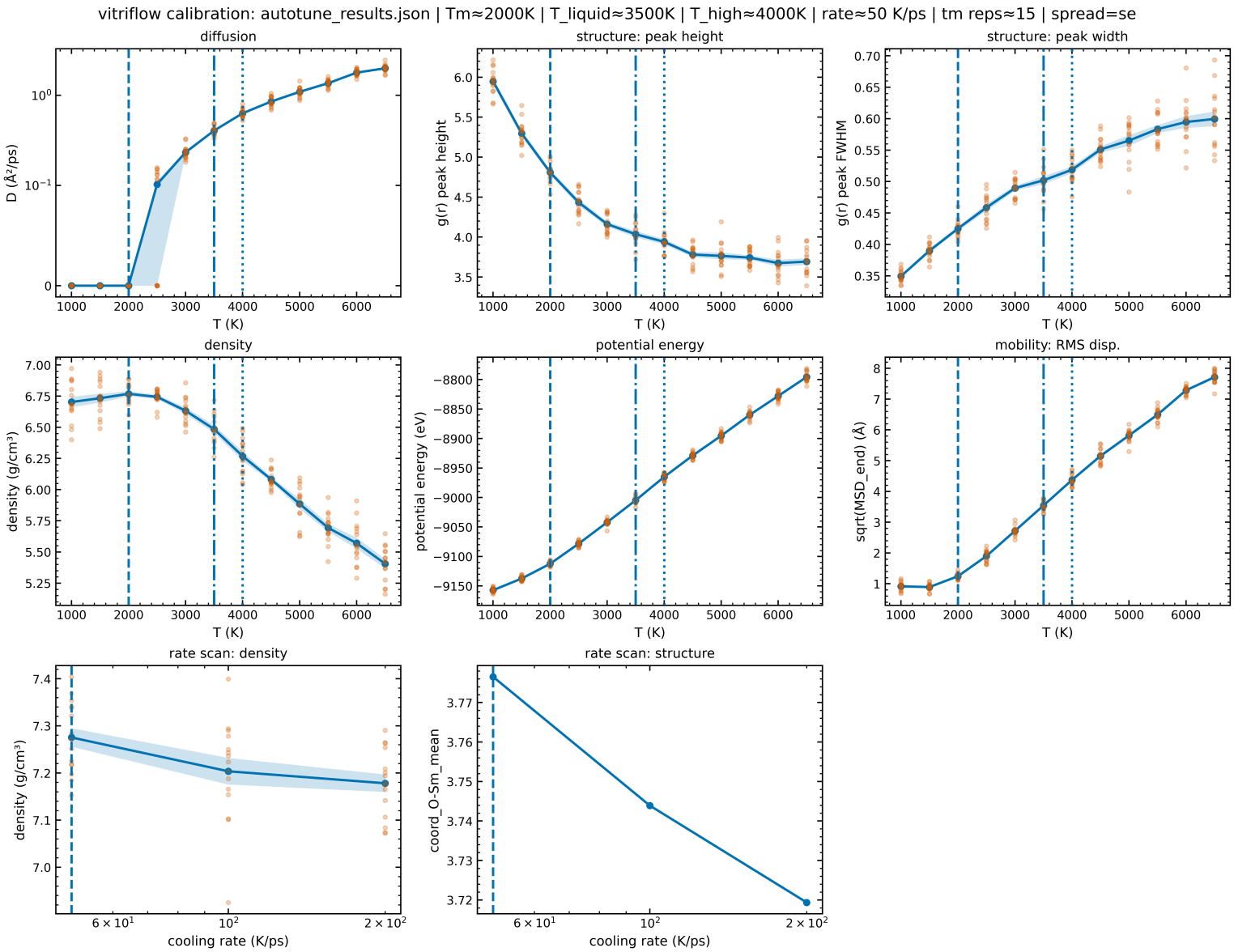

Figure S8: a-Sm_2O_3 `Vitriflow` calibration scan.

References

[1] M. P. Allen, D. J. Tildesley, Computer Simulation of Liquids, 2nd Edition, Oxford University Press, Oxford, 2017. doi:10.1093/oso/9780198803195.001.0001.

[2] H. E. Fischer, A. C. Barnes, P. S. Salmon, Neutron and x-ray diffraction studies of liquids and glasses, Reports on Progress in Physics 69 (1) (2006) 233–299. doi:10.1088/0034-4885/69/1/R05.

[3] D. S. Franzblau, Computation of ring statistics for network models of solids, Physical Review B 44 (10) (1991) 4925–4930. doi:10.1103/PhysRevB.44.4925.

[4] P. J. Steinhardt, D. R. Nelson, M. Ronchetti, Bond-orientational order in liquids and glasses, Physical Review B 28 (2) (1983) 784–805. doi:10.1103/PhysRevB.28.784.

[5] W. Lechner, C. Dellago, Accurate determination of crystal structures based on averaged local bond order parameters, The Journal of Chemical Physics 129 (11) (2008) 114707. doi:10.1063/1.2977970.

[6] S. Nosé, A unified formulation of the constant temperature molecular dynamics methods, The Journal of Chemical Physics 81 (1) (1984) 511–519. doi:10.1063/1.447334.

[7] W. G. Hoover, Canonical dynamics: Equilibrium phase-space distributions, Physical Review A 31 (3) (1985) 1695–1697. doi:10.1103/PhysRevA.31.1695.

[8] M. Parrinello, A. Rahman, Crystal structure and pair potentials: A molecular-dynamics study, Physical Review Letters 45 (14) (1980) 1196–1199. doi:10.1103/PhysRevLett.45.1196.

[9] G. J. Martyna, D. J. Tobias, M. L. Klein, Constant pressure molecular dynamics algorithms, The Journal of Chemical Physics 101 (5) (1994) 4177–4189. doi:10.1063/1.467468.

[10] H. Kim, B. Fábián, G. Hummer, Neighbor list artifacts in molecular dynamics simulations, Journal of Chemical Theory and Computation 19 (23) (2023) 8919–8929. doi:10.1021/acs.jctc.3c00777.

[11] R. A. Buckingham, The classical equation of state of gaseous helium, neon and argon, Proceedings of the Royal Society of London A 168 (933) (1938) 264–283. doi:10.1098/rspa.1938.0173.

[12] J. F. Ziegler, J. P. Biersack, U. Littmark, The Stopping and Range of Ions in Solids, Pergamon Press, New York, 1985.

[13] Student, The probable error of a mean, Biometrika 6 (1) (1908) 1–25. doi:10.1093/biomet/6.1.1.

[14] W. Hoeffding, Probability inequalities for sums of bounded random variables, Journal of the American Statistical Association 58 (301) (1963) 13–30. doi:10.1080/01621459.1963.10500830.

[15] A. Maurer, M. Pontil, Empirical bernstein bounds and sample variance penalization, arXiv:0907.3740 (2009). doi:10.48550/arXiv.0907.3740.

[16] C. Villani, Optimal Transport: Old and New, Vol. 338 of Grundlehren der mathematischen Wissenschaften, Springer, Berlin, Heidelberg, 2009. doi:10.1007/978-3-540-71050-9.

[17] F. J. Massey Jr., The kolmogorov-smirnov test for goodness of fit, Journal of the American Statistical Association 46 (253) (1951) 68–78. doi:10.1080/01621459.1951.10500769.

[18] S. Sundararaman, L. Huang, S. Ispas, W. Kob, New optimization scheme to obtain interaction potentials for oxide glasses, The Journal of Chemical Physics 148 (19) (2018) 194504. doi:10.1063/1.5023707.

[19] C. M. Marian, M. Gastreich, J. D. Gale, Empirical two-body potential for solid silicon nitride, boron nitride, and borosilazane modifications, Physical Review B 62 (5) (2000) 3117–3124. doi:10.1103/PhysRevB.62.3117.

[20] J. P. Perdew, K. Burke, M. Ernzerhof, Generalized gradient approximation made simple, Physical Review Letters 77 (18) (1996) 3865–3868. doi:10.1103/PhysRevLett.77.3865.

[21] J. Heyd, G. E. Scuseria, M. Ernzerhof, Hybrid functionals based on a screened coulomb potential, The Journal of Chemical Physics 118 (18) (2003) 8207–8215. doi:10.1063/1.1564060.

[22] J. Heyd, G. E. Scuseria, M. Ernzerhof, Erratum: "hybrid functionals based on a screened coulomb potential" [J. Chem. Phys. **118**, 8207 (2003)], The Journal of Chemical Physics 124 (21) (2006) 219906. doi:10.1063/1.2204597.

[23] A. V. Krukau, O. A. Vydrov, A. F. Izmaylov, G. E. Scuseria, Influence of the exchange screening parameter on the performance of screened hybrid functionals, The Journal of Chemical Physics 125 (22) (2006) 224106. doi:10.1063/1.2404663.